





Serpentinite Dehydration and Olivine Vein Formation During Ductile Shearing: Insights From 2D Numerical Modeling on Porosity Generation, Density Variations, and Transient Weakening

Stefan M. Schmalholz¹ , Evangelos Moulas², Ludovic Räss^{3,4,5} , and Othmar Müntener¹

¹Institute of Earth Sciences, University of Lausanne, Lausanne, Switzerland, ²Institut of Geosciences and Mainz Institute of Multiscale Modeling (M³ODEL), Johannes Gutenberg University of Mainz, Mainz, Germany, ³Laboratory of Hydraulics, Hydrology and Glaciology (VAW), ETH Zurich, Zurich, Switzerland, ⁴Swiss Federal Institute for Forest, Snow and Landscape Research (WSL), Birmensdorf, Switzerland, ⁵Now at Institute of Earth Sciences, University of Lausanne, Lausanne, Switzerland

Key Points:

- During ductile simple shearing of serpentinite, dehydration forms en échelon olivine veins that grow in direction parallel to compression
- Shear-driven fluid pressure perturbations trigger dehydration and large density changes in a 2D hydro-mechanical-chemical model
- We quantify porosity generation resulting from changes in solid volume and density, and from reactive mass transfer

Correspondence to:

S. M. Schmalholz,
stefan.schmalholz@unil.ch

Citation:

Schmalholz, S. M., Moulas, E., Räss, L., & Müntener, O. (2023). Serpentinite dehydration and olivine vein formation during ductile shearing: Insights from 2D numerical modeling on porosity generation, density variations, and transient weakening. *Journal of Geophysical Research: Solid Earth*, 128, e2023JB026985. <https://doi.org/10.1029/2023JB026985>

Received 26 APR 2023

Accepted 15 OCT 2023

Author Contributions:

Conceptualization: Stefan M. Schmalholz

Data curation: Stefan M. Schmalholz

Formal analysis: Stefan M. Schmalholz

Investigation: Stefan M. Schmalholz, Evangelos Moulas

Methodology: Stefan M. Schmalholz, Evangelos Moulas

Resources: Stefan M. Schmalholz, Othmar Müntener

Software: Stefan M. Schmalholz, Evangelos Moulas, Ludovic Räss

Validation: Stefan M. Schmalholz, Evangelos Moulas, Ludovic Räss, Othmar Müntener

© 2023. The Authors.

This is an open access article under the terms of the [Creative Commons Attribution-NonCommercial-NoDerivs License](https://creativecommons.org/licenses/by-nc-nd/4.0/), which permits use and distribution in any medium, provided the original work is properly cited, the use is non-commercial and no modifications or adaptations are made.

Abstract Serpentinite dehydration is important for subduction zone dynamics and water cycling. Field observations suggest that en échelon olivine veins in serpentinite mylonites formed by dehydration during simultaneous shearing of antigorite serpentinite. Here, we test the hypothesis of shear-driven formation of olivine dehydration veins with a novel two-dimensional hydro-mechanical-chemical numerical model. Our model accounts for the reaction antigorite + brucite = forsterite + water, considering significant solid density changes of approximately 25%. We assume ductile shearing, a decrease of shear viscosity with increasing porosity, and initially homogeneous total and fluid pressures within the serpentinite stability field. Initial perturbations in porosity, and hence viscosity, cause fluid pressure perturbations during simple shearing. Dehydration nucleates where fluid pressure locally drops below the thermodynamic pressure controlling the reaction boundary. During shearing, dehydration veins grow and serpentinite transforms into olivine inside the veins. Simulations show that the ambient pressure and the relation between compaction length and porosity have a major impact on vein formation. Conversely, the orientation of the initial porosity perturbation, the pressure-insensitive yield stress, the porosity dependence of compaction viscosity, the elastic effects during compaction, and the reaction kinetics have minor impacts on the simulations. We quantify the relative contribution of the rates of solid volume change, solid density change, and reactive mass transfer to the porosity generation. Vein growth is self-limiting and eventually reaches a steady state. We discuss potential implications for natural olivine veins, slow slip and tremor, transient weakening, anisotropy generation, and formation of shear-driven high-porosity bands without a dehydration reaction.

Plain Language Summary Serpentinite is a rock that contains water which is bound within the crystal lattice. When a tectonic plate brings serpentinite down into the Earth's mantle, the changing pressure and temperature conditions cause chemical reactions that release the water bound in the crystal lattice; a process called dehydration. A typical mineral that forms by serpentine dehydration is olivine. Dehydration is important for the global deep-water cycle since much water is transferred with tectonic plates into the mantle and migrates back to the Earth's surface after dehydration. However, many aspects of the water cycle remain still unclear, since dehydration during the plunging of tectonic plates involves the incompletely understood interaction of three fundamental mechanical and chemical processes: mechanical deformation of the rock, porous flow of released fluid, and chemical reactions involving changes in rock density. Here, we present a new mathematical model to investigate the coupled processes of rock deformation, fluid flow, and dehydration reactions. We present computer simulations that can explain why the dehydration occurs in narrow and elongated regions which are termed veins. We propose that our simulations could explain the field observation of many small olivine veins in strongly sheared serpentinite.

1. Introduction

The dehydration of serpentinite at subduction zones plays a crucial role in the global deep water cycle (e.g., Peacock, 1990; Pettke & Bretscher, 2022; Rupke et al., 2004; Ulmer & Trommsdorff, 1995), subduction zone dynamics and seismicity (e.g., Bloch et al., 2018; Hacker et al., 2003) and arc magmatism due to mantle wedge

Visualization: Stefan M. Schmalholz
Writing – original draft: Stefan M. Schmalholz, Evangelos Moulas, Ludovic Räss, Othmar Müntener

hydration (e.g., Hebert et al., 2009; John et al., 2012). The coupling of metamorphic reactions, fluid flow, and rock deformation is crucial for various geodynamic processes. These include chemical and volatile cycling (e.g., Bebout, 2014), reaction-induced weakening of faults and shear zones (e.g., Labrousse et al., 2010; Sulem & Famin, 2009), and practical applications like carbon storage (e.g., Matter & Kelemen, 2009) and geothermal energy exploitation (e.g., Pandey et al., 2018). However, the coupling of metamorphic reactions, fluid flow, and rock deformation remains unclear in many aspects.

Indirect observations that have been attributed to serpentinite dehydration at subduction zones are aseismic episodic tremor and slow slip (ETS) phenomena (e.g., Behr & Bürgmann, 2021; Burlini et al., 2009; Tarling et al., 2019). These phenomena are commonly thought to result from episodic fault slip, likely promoted by pulses of fluid release associated with fluid pressure variations (e.g., Audet et al., 2009; Connolly, 1997; Frank et al., 2015; Gomberg et al., 2010; Shelly et al., 2007; Taetz et al., 2018). For example, such slow slip occurs on the plate interface in Cascadia at 30–40 km depth (e.g., Gomberg et al., 2010) and for temperatures probably between 400 and 500°C (e.g., Tarling et al., 2019 and references therein).

Direct observation of the dehydration of serpentinite at subduction zones is not possible in nature so we must use exposed serpentinites on the surface as proxies for the reacted materials. Field observations in areas with abundant exposed serpentinites, formed at variable pressure and temperature, may, hence, provide insight into incipient dehydration stages. Exposed serpentinites are abundant in many regions of the European Alps, having undergone variable peak pressures and temperatures. Examples are the antigorite serpentinites of Saas Zermatt (Western Alps) and the Erro-Tobbio unit (Voltri massif, Ligurian Alps, Italy; e.g., Hermann et al., 2000; Kempf et al., 2020; Peters et al., 2020; Plümper et al., 2017; Scambelluri et al., 1991, 1995). These serpentinite-bearing regions are key areas that preserve ductile and brittle structures that are synchronous to fluid release. The antigorite serpentinites of the Erro-Tobbio unit include olivine-bearing veins (Figure 1). The olivine is most likely metamorphic olivine that was formed by the breakdown of antigorite and brucite (e.g., Hermann et al., 2000; Plümper et al., 2017; Scambelluri et al., 2004). The serpentinites were initially formed by hydration of the subcontinental mantle which was exposed to the Tethyan ocean floor during pre-Alpine extension (e.g., Scambelluri et al., 1995). During later Alpine subduction, the serpentinites underwent prograde metamorphism and transformed to antigorite serpentinites (e.g., Scambelluri et al., 2004; see also our Figure 2). During subduction, the serpentinites, containing likely a small amount of olivine, have been sheared generating antigorite serpentinite mylonites (e.g., Scambelluri et al., 1995; our Figure 2). The exhumed antigorite mylonites are dissected by en échelon olivine veins (e.g., Scambelluri et al., 1995; our Figure 1). The olivine-bearing antigorite serpentinites in the Erro Tobbio region indicate that they underwent the brucite-out reaction during subduction, allowing for olivine formation, but did not undergo the antigorite-out reaction before exhumation (e.g., Scambelluri et al., 1995; our Figure 2e). Most likely, the olivine veins were formed by the breakdown of mainly brucite when the subducting and actively deforming antigorite serpentinite underwent the brucite-out reaction (Figure 2e).

The olivine veins occur in two settings: as minimally deformed veins within little deformed, variably serpentinitized peridotite and as deformed veins within strongly deformed antigorite serpentinite, described as a serpentinite mylonite (our Figure 1; e.g., Hermann et al., 2000; Plümper et al., 2017). These serpentinite mylonites are cut by en échelon olivine veins, which in turn are dissected by multiple sets of olivine-bearing shear bands (Hermann et al., 2000). Plümper et al. (2017) suggested that the association of undeformed and sheared veins attests that dehydration-induced vein formation was synchronous with ductile deformation in the enclosing serpentinite mylonites. Furthermore, Hermann et al. (2000) hypothesized that (a) multiple sets of olivine shear bands provide evidence for continuous deformation, (b) sheared olivine-rich veins are probably very weak due to continuous solution and precipitation in the presence of a fluid phase, (c) fluid produced by the dehydration reaction was (partially) trapped in the serpentinite mylonite and (d) serpentinite mylonites are not only zones with highly localized deformation but they are also zones of focused fluid flow. These hypotheses for olivine vein formation imply the coupling of certain mechanical, hydrological, and chemical mechanisms, but these hypotheses have not been tested yet with theoretical models and numerical simulations based on the concepts of continuum mechanics and thermodynamics.

Here, we test a hypothesis for olivine vein formation by using a theoretical model considering the coupling of metamorphic reactions, fluid flow, and rock deformation. We refer to such coupled model as hydro-mechanical-chemical (HMC) model (e.g., Kolditz et al., 2016; Poulet et al., 2012). Such HMC models have been applied to study a variety of geodynamic processes, such as reaction-driven cracking during serpentinitization (e.g., O. Evans

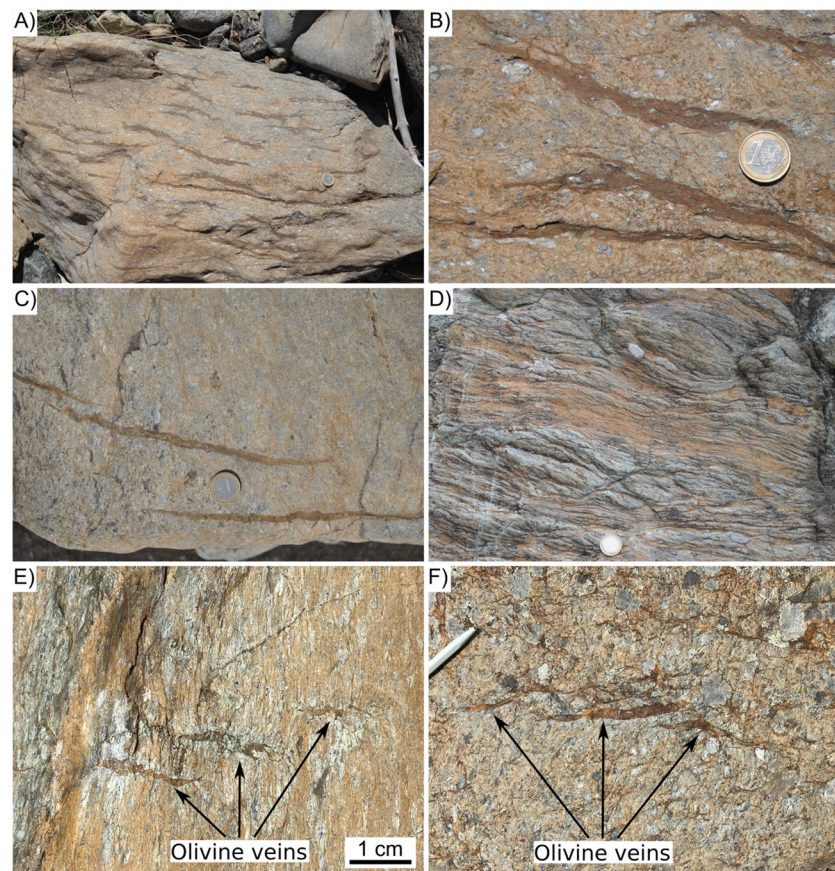


Figure 1. Natural examples of metamorphic olivine veins in antigorite serpentinite from the Erro Tobbio ultramafic rocks, Ligurian Alps, Italy. (a) Overview on the limited spatial extent of olivine bearing veins (with darker color) in weakly deformed serpentinitized peridotite. Coin diameter is 2.4 cm. (b) Olivine veins with characteristic spacing and aspect ratios in serpentinitized peridotite. (c) Olivine-bearing veins in a serpentinitized peridotite, foliation is sub vertical, extent of veins is ca. 20 cm. (d) Serpentinite mylonite with different generations of olivine veins. An earlier set is subparallel to the foliation, younger shear bands dissect serpentinite mylonite and olivine veins. The structures indicate a top-to-the-left shear sense. Note the late-stage serpentine veins that are perpendicular to the foliation. (e) and (f) En échelon olivine veins in antigorite serpentinite. Coordinates: (a) and (b) at 44.56081°N, 8.81376°E; (c) at 44.57147°N, 8.80825°E; (d) at 44.56958°N, 8.80814°E; (e) and (f) at 44.57140°N, 8.80784°E. All photos have been taken by S. Schmalholz and O. Müntener in summer 2022.

et al., 2020), porosity evolution and clogging during serpentinization (e.g., Malvoisin et al., 2021), the impact of dehydration on earthquake nucleation (e.g., Brantut et al., 2011), the impact of shear heating and associated chemical rock decomposition on thrusting (e.g., Poulet et al., 2014) and reactive melt migration (e.g., Aharonov et al., 1997; Baltzell et al., 2015; Bessat et al., 2022; Keller & Katz, 2016; Schiemenz et al., 2011). Several HMC models exist for melt migration which account for the interaction between reactions, fluid flow, and solid deformation (e.g., Katz, 2008; Keller & Katz, 2016; Schiemenz et al., 2011). Most of these models, however, assume that the densities of the solid and fluid constituents remain constant during deformation and reaction (e.g., Katz, 2008; Keller & Katz, 2016; Schiemenz et al., 2011). Given the considerable changes in the densities of the reacting and deforming rocks, these models are not suitable for studying metamorphic reactions, like the serpentinite to olivine reaction (e.g., Malvoisin et al., 2015). Recently, Huber et al. (2022) presented a hydro-chemical model to study the formation of olivine veins in dehydrating serpentinite considering density changes. However, they do not consider any solid-mechanical aspects of olivine vein formation and hence, do not consider volumetric or shear deformation and associated fluid pressure changes. O. Evans et al. (2018, 2020) presented a numerical HMC model to study serpentinization and associated reaction-driven cracking. They consider elastic deformation and do not consider the spatial and temporal variation in solid density. Therefore, most existing HMC models are not appropriate for studying olivine vein formation caused by dehydration of serpentinite during ductile shearing.

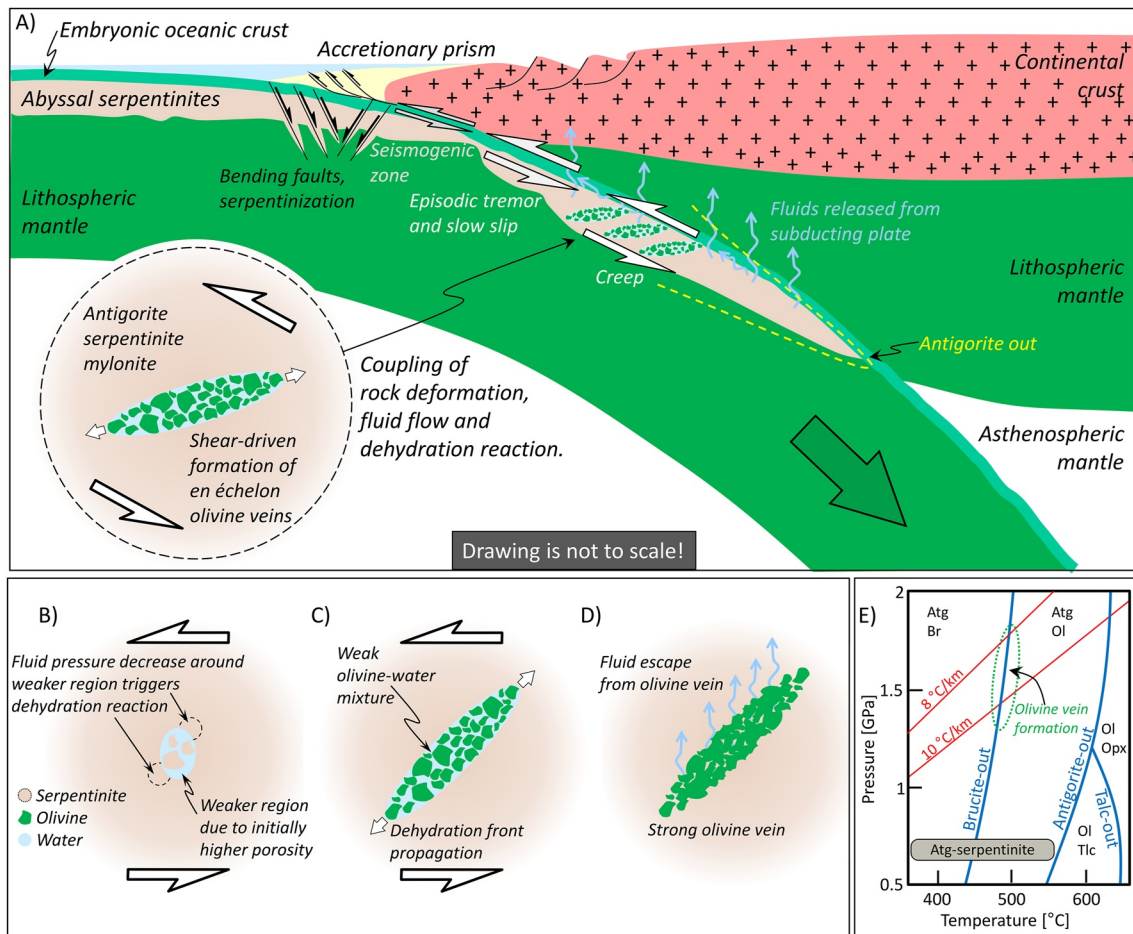


Figure 2. Simple sketches illustrating the geodynamic setting (a) and the hypothesis for shear-driven dehydration and olivine vein formation in viscous serpentinite (b–d; see text for details). The drawing is not to scale. (e) Simplified phase diagram showing the brucite-out and antigorite-out reactions, two common subduction geotherms (in °C/km), the likely region of olivine vein formation (green dashed ellipse) and typical minerals. The phase diagram is simplified for a MSH system after Figure 6 in Padrón-Navarta et al. (2013). Mineral abbreviations: Atg, antigorite; Br, brucite; Ol, olivine; Opx, orthopyroxene; and Tlc, talc.

Here, we develop a novel two-dimensional (2D) HMC model that can numerically simulate the formation of dehydration veins in viscously shearing serpentinite while taking into account the significant spatial and temporal variations in solid density resulting from the dehydration reaction. We follow and elaborate the theoretical model of Malvoisin et al. (2015) which investigates the coupling of metamorphic reactions, fluid flow, and volumetric rock deformation. This model accounts for spatial and temporal variations in fluid and solid densities, which are calculated using equilibrium thermodynamics and Gibbs energy minimization (e.g., Malvoisin et al., 2015). Based on this model, Schmalholz et al. (2020) developed a 2D HMC model to numerically simulate the coupling between viscous rock deformation, fluid flow, and the dehydration reaction: brucite = periclase + water. Here, we elaborate this HMC model and consider a simple MgO-SiO₂-H₂O (MSH) system for the reaction: antigorite + brucite = forsterite + water (e.g., B. W. Evans, 2004; our Figure 3). For simplicity, we consider an isothermal system and a fixed chemical composition so that the reaction antigorite + brucite = forsterite + water is balanced everywhere in the model domain.

With our new HMC model, we evaluate the following process hypothesis (Figure 2): There are zones in a subduction setting where serpentinite is undergoing viscous shear near the ambient pressure and temperature conditions that can trigger the dehydration reaction from serpentinite to olivine (Figures 2e and 3a). The effective viscosity of serpentinite is spatially variable, for example, due to variable porosity or heterogeneities in mineralogy (Figure 2b). Domains with lower viscosity cause pressure variations in serpentinite resulting in locally decreased pressure compared to ambient pressure. If the pressure decreases below the reaction pressure in certain domains, it triggers the dehydration reaction in those domains. The formation of olivine due to dehydration results in

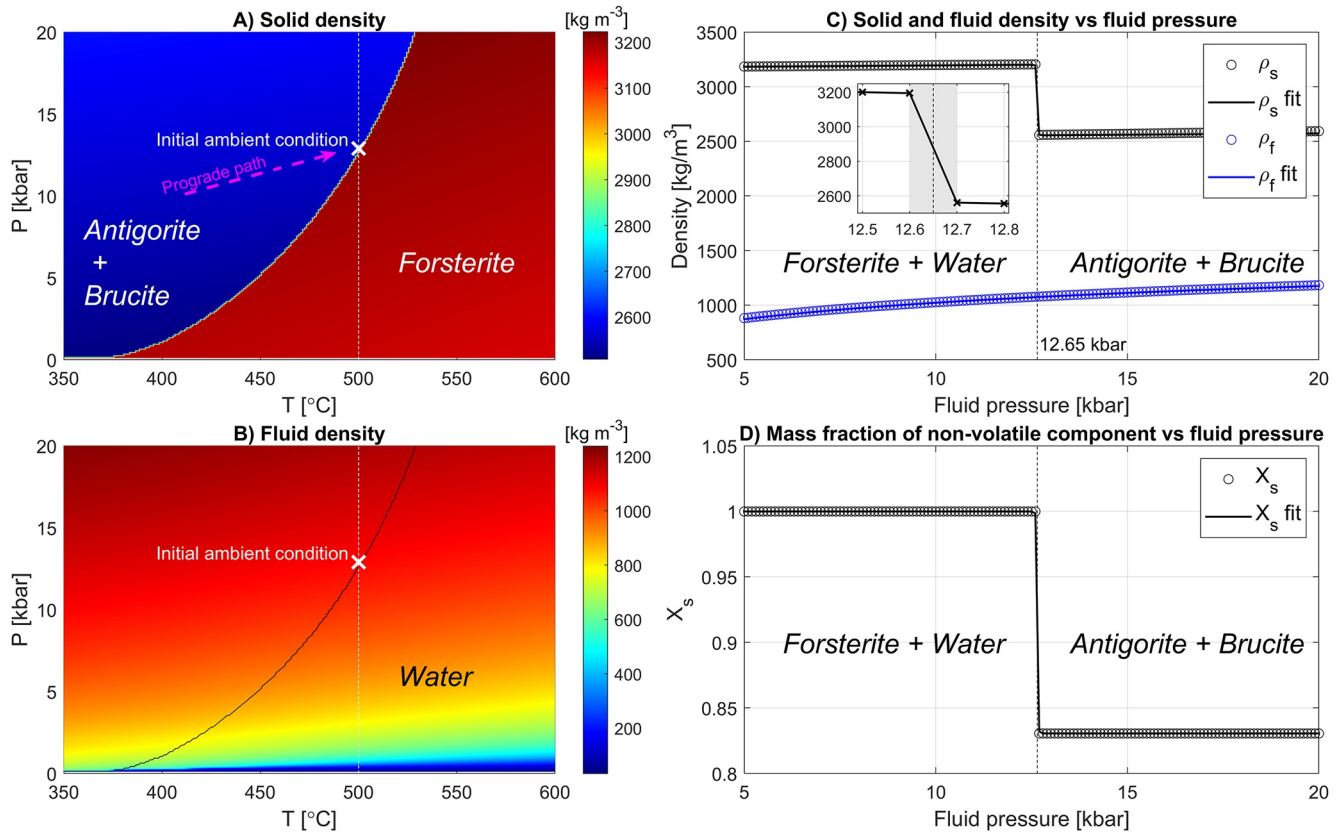


Figure 3. Thermodynamic results obtained from Gibbs' free energy minimization for the system antigorite + brucite = forsterite + water (see text for exact chemical formulas). Density fields of solid (a) and fluid (b) in thermodynamic pressure, P , and temperature, T , space. Corresponding profiles of solid and fluid densities (c) and mass fraction of the non-volatile solid component, $\text{MgO} + \text{SiO}_2$, (d) as a function of fluid pressure at 500°C. The circles in the three profiles in panels (c) and (d) are the results from Gibbs energy minimization and the corresponding solid lines are analytical approximations of these profiles, which are used in the numerical algorithm (see Appendix A1). Thermodynamic calculations are based on `Perple_X`.

increased porosity, leading to larger weak domains containing a mixture of olivine and fluid. The region of dehydration forms structures resembling veins that grow parallel to the direction of maximum compressive stress without fracturing (Figures 2b and 2c). Afterward, fluid is released from the area abundant in olivine, and veins rich in olivine are formed (Figure 2d).

The primary objective of our study is to investigate the fundamental coupling of dehydration, density changes, fluid flow, and rock deformation. To facilitate this study, we employ a simplified model. The specific goals of our study are: (a) Development of a 2D numerical HMC model capable of simulating the formation of olivine dehydration veins within viscously shearing serpentinite. This model must account for substantial spatial and temporal variations in solid density. (b) Evaluation of the hypothesis concerning the shear-driven genesis of olivine veins in antigorite serpentinite. (c) Quantification of the underlying mechanisms governing the evolution and generation of porosity during the dehydration of rocks experiencing ductile deformation.

2. Mathematical Model

2.1. Outline

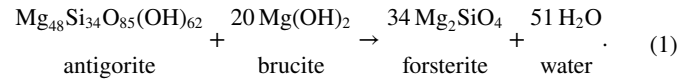
We begin by presenting the dehydration reaction and densities required for our HMC model. We then describe the thermodynamic calculation of densities and introduce mass conservation equations that use them. After that, we describe the hydrological model for porous flow, and the mechanical model for solid deformation including the constitutive, rheological equations. Finally, we present the governing system of equations and the numerical algorithm used to solve them.

Table 1
Symbols Used in the Text

Symbol	Name/Definition	Units
r	Bandwidth of Gaussian	[m]
w	Model width	[m]
x, y	Spatial coordinates	[m]
δ	Compaction length	[m]
k	Permeability	[m ²]
t	Time	[s]
t_c	Characteristic time	[s]
t_{kin}	Kinetic time	[s]
t_{Max}	Maxwell time	[s]
\overline{D}_{xy}	Far-field shearing rate	[s ⁻¹]
u_x^s, v_y^s	Solid velocities	[m·s ⁻¹]
u_x^f, v_y^f	Fluid velocities	[m·s ⁻¹]
p_f	Fluid pressure	[Pa]
p	Total pressure	[Pa]
p_a	Ambient pressure	[Pa]
p_r	Reaction pressure	[Pa]
$\sigma_{xx}, \sigma_{yy}, \sigma_{xy}$	Total stresses	[Pa]
$\tau_{xx}, \tau_{yy}, \tau_{xy}$	Deviatoric stresses	[Pa]
τ_{II}	Deviatoric stress invariant	[Pa]
K_s	Bulk modulus solid	[Pa]
K_d	Bulk modulus drained	[Pa]
η_f	Fluid viscosity	[Pa·s]
η_s	Shear viscosity solid	[Pa·s]
ζ	Compaction viscosity	[Pa·s]
ρ_s	Solid density	[kg·m ⁻³]
ρ_f	Fluid density	[kg·m ⁻³]
Γ	Mass transfer rate	[kg·m ⁻³ ·s ⁻¹]
ϕ	Porosity	[]
ϕ_a	Ambient porosity	[]
ϕ_0	Initial porosity	[]
X_s	Mass fraction of MgO + SiO ₂	[]
a	Parameter in η_s versus ϕ relation	[]
n	Exponent in η_s versus ϕ relation	[]
α	Biot-Willis coefficient	[]
$\Omega_{1,2,3,4,5,6}$	Dimensionless parameters; Equation 29	[]

2.2. Reaction, Densities, and Mass Fraction

We consider a simple MSH system and the dehydration reaction (e.g., B. W. Evans, 2004; Padrón-Navarta et al., 2013):



From a hydromechanical point of view, this reaction occurs in a two-phase system composed of a solid phase and a free porous fluid phase. The four thermodynamic phases considered are antigorite, brucite, forsterite, and water. MgO, SiO₂, and H₂O represent the three chemical components. The free porous fluid phase is H₂O with pore-fluid density ρ_f (in kg/m³). All symbols used in the text are explained in Table 1. The solid rock phase consists either of forsterite or antigorite + brucite. We assume that antigorite + brucite together represent one solid rock “phase” with a homogeneous solid density, ρ_s , and homogeneous material properties. The ρ_s in the reactive two-phase system is, hence, either the density of forsterite or of antigorite + brucite. This assumption is consistent with the theories of multiphase flow where rock properties such as density or viscosity are average properties and apply for regions larger than the rock’s grain size (e.g., McKenzie, 1984). The total density of the porous two-phase rock is

$$\rho_T = \rho_f \phi + \rho_s(1 - \phi), \quad (2)$$

with the porosity ϕ (volume ratio). The solid phase can consist of three chemical components, the two solid non-volatile components, MgO and SiO₂, that remain always in the solid, and the volatile component, H₂O, that is structurally bound in the solid made of antigorite + brucite and liberated during dehydration. Together, MgO and SiO₂ represent a single non-volatile solid component in the solid phase that either consists of forsterite or antigorite + brucite. We quantify the mass (in kg) fraction, X_s , of the non-volatile solid component inside the solid phase. For forsterite, $X_s = 1.0$ because forsterite is made only of the non-volatile solid component, MgO + SiO₂. To calculate X_s for the solid phase made of antigorite + brucite, we need to specify the molar masses, M , of the three chemical components: For MgO, $M_{MgO} = 0.04$ kg/mol, for SiO₂, $M_{SiO_2} = 0.06$ kg/mol, and for H₂O, $M_{H_2O} = 0.018$ kg/mol. The molar masses of the chemical components can be calculated from the atomic weights of the chemical elements involved. These atomic weights are available, for example, from online tables of various commissions, such as the Commission on Isotopic Abundances and Atomic Weights (iupac.qmul.ac.uk/AtWt). Equation 1 indicates how many of the chemical components of MgO, SiO₂, and H₂O are within the solid phase made of antigorite + brucite. The mass fraction of the non-volatile solid component, MgO + SiO₂, in the solid phase made of antigorite + brucite is then given by:

$$X_s = \frac{68M_{MgO} + 34M_{SiO_2}}{68M_{MgO} + 34M_{SiO_2} + 51M_{H_2O}} \approx 0.84. \quad (3)$$

The relative density of the non-volatile solid component, MgO + SiO₂, in the solid phase made of antigorite + brucite, is

$$\rho_X = \rho_s X_s. \quad (4)$$

We use the relative density, ρ_X , later to formulate the mass conservation equation for the non-volatile solid component, MgO + SiO₂.

2.3. Thermodynamics and Kinetics

We consider local thermodynamic equilibrium, a constant temperature, and a closed system with constant system composition for the entire model domain. The composition is constant with respect to the non-volatile solid components, MgO and SiO₂, and H₂O can migrate in the model domain. It has been theoretically and experimentally demonstrated that metamorphic reactions in solid-fluid systems are controlled by fluid pressure, p_f (e.g., Dahlen, 1992; Llana-Fúnez et al., 2012). Therefore, we approximate ρ_s , ρ_f , and X_s as a function of p_f which is expressed as (e.g., Schmalholz et al., 2020):

$$\begin{aligned}\rho_f &= \rho_f^{EQ}(p_f) \\ \rho_s &= \rho_s^{EQ}(p_f), \\ X_s &= X_s^{EQ}(p_f)\end{aligned}\quad (5)$$

whereby the values of ρ_s^{EQ} , ρ_f^{EQ} , and X_s^{EQ} for a range of values of p_f are calculated by equilibrium Gibbs free-energy minimization using the program `Perple_X` (e.g., Connolly, 1990, 2005, 2009; our Figure 3), utilizing the thermodynamic data set of Holland and Powell (1998). Newer thermodynamic data sets do not differ considerably from the Holland and Powell (1998) data set concerning Gibbs free energies and the associated densities of the minerals considered here. We assume that ρ_f always corresponds to ρ_f^{EQ} , because of its equation of state (Figure 3c).

Due to the considerably sharp, step-like variation of ρ_s^{EQ} and X_s^{EQ} with varying p_f across the dehydration reaction (Figures 3c and 3d), we assume that the reaction can involve a kinetic reaction timescale. We apply the kinetic model of Omlin et al. (2017) which represents simple, first-order reaction kinetics. If p_f changes, then the values of ρ_s and X_s are not instantaneously assigned to the corresponding values of ρ_s^{EQ} and X_s^{EQ} , but there is a kinetic time delay to reach the values of ρ_s^{EQ} and X_s^{EQ} . The first-order reaction kinetics relevant to the thermodynamic equilibrium are (e.g., Omlin et al., 2017)

$$\begin{aligned}\frac{\partial \rho_s}{\partial t} &= \frac{\rho_s^{EQ} - \rho_s}{t_{kin}} \\ \frac{\partial X_s}{\partial t} &= \frac{X_s^{EQ} - X_s}{t_{kin}},\end{aligned}\quad (6)$$

where t_{kin} is the characteristic kinetic timescale. For simplicity, we assume that t_{kin} is constant. Our kinetic model is similar to first-order linear kinetic models, for example, applied to study reaction-infiltration instabilities, in which the mass transfer rate is proportional to the difference between an equilibrium concentration and the actual concentration of a component (e.g., Aharonov et al., 1995, 1997; Jones & Katz, 2018; Spiegelman et al., 2001). In contrast to our model, these models assume that ρ_s is constant during the reaction and therefore do not consider any change of ρ_s during the reaction progress.

2.4. Mass Conservation

For two-phase systems, the conservation of mass (per unit volume) of the solid and the fluid is frequently given by the respective equations (e.g., McKenzie, 1984)

$$\frac{\partial(\rho_s(1-\phi))}{\partial t} + \nabla \cdot (\rho_s(1-\phi)\mathbf{v}^s) = -\Gamma \quad (7)$$

$$\frac{\partial(\rho_f\phi)}{\partial t} + \nabla \cdot (\rho_f\phi\mathbf{v}^f) = \Gamma, \quad (8)$$

where t is time, $\nabla \cdot$ is the divergence operator, \mathbf{v}^f and \mathbf{v}^s are vectors of the fluid and solid barycentric velocities, respectively, and Γ is a mass transfer rate from the solid to the fluid phase. Concerning the symbols for vector and tensor quantities, we use indices f and s as superscripts, because vector and tensor components will have additional subscripts indicating the spatial direction, and scalar quantities can be easily distinguished from vector and tensor quantities. In our mathematical model, we do not use two mass conservation equations in the form of Equations 7 and 8. Instead, we employ two different forms of the mass conservation equations: a conservation equation for total mass and a conservation equation for the mass of the total solid non-volatile component,

MgO + SiO₂. The conservation equation of total mass results from the sum of Equations 7 and 8 (e.g., Beinlich et al., 2020; Fowler, 1985; Malvoisin et al., 2021; Plümper et al., 2017; Schmalholz et al., 2020):

$$\frac{\partial \rho_T}{\partial t} + \nabla \cdot (\rho_f \phi (\mathbf{v}^f - \mathbf{v}^s)) + \nabla \cdot (\rho_T \mathbf{v}^s) = 0. \quad (9)$$

The conservation equation for the total non-volatile component, MgO + SiO₂, is (e.g., Plümper et al., 2017; Schmalholz et al., 2020)

$$\frac{\partial}{\partial t} (\rho_X (1 - \phi)) + \nabla \cdot (\rho_X (1 - \phi) \mathbf{v}^s) = 0. \quad (10)$$

There is no fluid velocity in the conservation Equation 10 because we assume that the dissolution of MgO and SiO₂ in the fluid is negligible. The main reason why we use mass conservation Equations 9 and 10, instead of Equations 7 and 8, is that Equations 9 and 10 do not include the term for the mass transfer rate, Γ . Therefore, we do not need to provide an expression for Γ .

2.5. Porous Flow

We apply Darcy's law to describe the porous flow of the free fluid phase. For simplicity, we consider porous flow in the absence of gravity for which Darcy's law is:

$$\phi (\mathbf{v}^f - \mathbf{v}^s) = -\frac{k \phi^3}{\eta_f} \nabla p_f, \quad (11)$$

where ∇ is the gradient operator, k is the permeability coefficient in a porosity-dependent, Kozeny-Carman-type permeability expression and η_f is the fluid viscosity.

2.6. Solid Deformation

The equations for the conservation of total linear momentum (or force balance equations) of the two-phase mixture without inertial forces and gravity are:

$$\nabla \cdot \sigma_{ij} = 0. \quad (12)$$

Subscripts i and j are either 1 (representing the horizontal x -direction) or 2 (representing the vertical y -direction). The components of the total stress tensor of the two-phase mixture, σ_{ij} , are composed of the total pressure, p , and the components of the total deviatoric stress tensor, τ_{ij} , by the relation

$$\sigma_{ij} = -p \delta_{ij} + \tau_{ij}, \quad (13)$$

with δ_{ij} being the Kronecker delta (e.g., Steeb & Renner, 2019). We assume that the contribution of fluid flow to the total deviatoric stress of the mixture is negligible and only consider the solid deformation in the calculation of the total deviatoric stress (e.g., McKenzie, 1984; Steeb & Renner, 2019). We consider a visco-plastic solid and the effective shear viscosity, η_s , relates the total deviatoric stress tensor components to the deviatoric strain rate tensor components of the solid, D_{ij} , by the equation:

$$\tau_{ij} = 2\eta_s D_{ij}, \quad (14)$$

with

$$D_{ij} = \frac{1}{2} \left(\frac{\partial v_i^s}{\partial x_j} + \frac{\partial v_j^s}{\partial x_i} \right) - \delta_{ij} \frac{1}{3} \frac{\partial v_k^s}{\partial x_k}. \quad (15)$$

Some studies apply the relation $\tau_{ij} = (1 - \phi) 2\eta_s D_{ij}$ to take into account that the solid deformation only contributes a part to the total deviatoric stress of the mixture (e.g., Keller et al., 2013), while other studies do not consider such porosity factor in the relation between total deviatoric stress of the two-phase mixture and partial deviatoric stress of the solid (e.g., Steeb & Renner, 2019). Here, we assume that such porosity effects are implicitly included in a porosity dependent η_s . The porosity dependence of η_s is motivated by studies on partially molten rocks (e.g.,

Katz et al., 2022; Mei et al., 2002; Schmeling et al., 2012). We consider here two types of porosity dependence of η_s , namely an exponential and a power-law dependence (e.g., Katz et al., 2006; Mei et al., 2002; Schmeling et al., 2012):

$$\eta_s = \eta_{s0} \exp(-a(\phi/\phi_0 - 1)) \quad (16)$$

$$\eta_s = \eta_{s0}(\phi_0/\phi)^n, \quad (17)$$

where η_{s0} is the reference shear viscosity for a reference porosity, ϕ_0 , and a and n are two parameters quantifying the dependence of η_s on ϕ . We further consider a von Mises yield stress, τ_y , to limit the maximal value of the deviatoric stresses. The square root of the second invariant of the deviatoric stress tensor, $\tau_{II} = \sqrt{0.5(\tau_{xx}^2 + \tau_{yy}^2) + \tau_{xy}^2}$, controls a plastic multiplier, $\vartheta = 1 - \tau_y/\tau_{II}$. If $\vartheta > 0$, then deviatoric stresses are modified using

$$\tau_{ij} = (1 - \vartheta)\tau_{ij}. \quad (18)$$

We use such a stress limiter in some numerical simulations to test if it significantly impacts the simulations of olivine vein formation. Another reason is that this pressure-insensitive yield stress can represent any strong nonlinear dependence of the shear viscosity on the deviatoric stress, such as for low-temperature plasticity or exponential creep (e.g., Karato, 2008; Schmalholz & Fletcher, 2011; Tsenn & Carter, 1987). For such exponential creep, the stress increases only slightly with increasing strain rate, in contrast to the linear viscosity, η_s , for which stresses increase linearly with strain rate, if ϕ is constant.

Furthermore, we consider a poro-visco-elastic volumetric deformation for which the divergence of the solid velocity field is a function of total pressure, p , and p_f (e.g., Yarushina & Podladchikov, 2015):

$$\nabla \cdot \mathbf{v}^s = -\frac{1}{K_d} \left(\frac{dp}{dt} - \alpha \frac{dp_f}{dt} \right) - \frac{p - p_f}{(1 - \phi)\zeta}, \quad (19)$$

where ζ is the compaction viscosity, K_d is the drained bulk modulus, and $\alpha = 1 - K_d/K_s$ with K_s being the solid bulk modulus. The magnitude of ζ is linked to the magnitude of η_s and the inverse of ϕ by the equation (e.g., Katz, 2008; Yarushina & Podladchikov, 2015)

$$\zeta = \Omega_4 \eta_s \frac{\phi_0}{\phi}. \quad (20)$$

The parameter $\Omega_4 = \zeta/\eta_s$ if $\phi = \phi_0$. We use the symbol Ω_4 because this parameter is one of several dimensionless numbers, we use later to characterize the numerical simulations. We consider visco-elastic bulk deformation because it can avoid unrealistically fast viscous compaction in case ζ is very small. The elasticity component delays the viscous compaction, and the characteristic time of the delay is controlled by a so-called Maxwell time that can be approximated for the applied Equation 20 by the ratio $t_{Max} = \zeta/K_d$. Furthermore, the poro-visco-elastic formulation provides the poro-elastic limit in case ζ is very large, for example, for regions with very small ϕ .

2.7. Governing System of Equations

The governing system of equations serves as the foundation for constructing the numerical algorithm that calculates the principal unknown quantities. For our model, we have 8 principal unknowns that are ρ_s , ρ_f , X_s , p_f , ϕ , p , v_x^s and v_y^s . Other quantities that need to be calculated, such as D_{ij}^s , τ_{ij}^s , and σ_{ij}^s , can be directly calculated from the 8 unknowns with equations presented above (see also below). The v_x^f and v_y^f do not appear as unknowns because we substitute Darcy's law, Equation 11, into the conservation equation for total mass, Equation 9, to eliminate v_x^f and v_y^f as unknowns.

To determine the eight unknowns, we need eight equations. Three equations to calculate the values of ρ_s , ρ_f and X_s are derived from equilibrium thermodynamic calculations. The ρ_s , ρ_f and X_s are calculated with p_f using the results of thermodynamic calculations (Figures 3c and 3d). Hence, the three equations relating ρ_s , ρ_f and X_s to p_f are calculated by `Perple_X` and are then used during the numerical simulations. The time evolution of ρ_s and X_s is calculated with Equation 6. The remaining five governing equations are the two mass conservation Equations 9

and 10, Equation 19 describing volumetric deformation, and the two momentum balance Equation 12. The system of 8 governing equations is:

$$\rho_f = \rho_f^{EQ}(p_f); \text{calculated by Perple_X} \quad (21)$$

$$\rho_s = \rho_s^{EQ}(p_f); \text{calculated by Perple_X} \quad (22)$$

$$X_s = X_s^{EQ}(p_f); \text{calculated by Perple_X} \quad (23)$$

$$\frac{\partial \rho_T}{\partial t} = \nabla \cdot \left[\rho_f \frac{k\phi^3}{\eta_f} \nabla p_f \right] - \nabla \cdot (\rho_T \mathbf{v}^s) \quad (24)$$

$$\frac{\partial}{\partial t} [\rho_s X_s (1 - \phi)] = -\nabla \cdot [\rho_s X_s (1 - \phi) \mathbf{v}^s] \quad (25)$$

$$\nabla \cdot \mathbf{v}^s = -\frac{1}{K_d} \left(\frac{dp}{dt} - \alpha \frac{dp_f}{dt} \right) - \frac{p - p_f}{(1 - \phi)\zeta} \quad (26)$$

$$\nabla \cdot \sigma_{ij} = 0 \quad (27)$$

Once the v_x^s and v_y^s are determined, the strain rates, D_{ij} , are calculated with Equation 15. The η_s are calculated with ϕ using Equations 16 or 17. The deviatoric stresses, τ_{ij} , are calculated with Equations 14, 16, and 17. The total stresses, σ_{ij} , are then calculated with p and τ_{ij} using Equation 13.

2.8. Numerical Algorithm

We discretize the system of differential Equations 6 and 24–27 using the finite difference method on a regular Cartesian staggered grid. The staggering relies on second-order conservative finite differences (e.g., McKee et al., 2008; Patankar, 2018; Virieux, 1986). We solve the discretized form of the five Equations 24–27 for the unknowns p_f , ϕ , p , v_x^s , and v_y^s with the accelerated pseudo-transient (PT) method in an iterative and matrix-free fashion (e.g., Chorin, 1997; Räss et al., 2022). We use a relaxation, or continuation, approach to handling the various nonlinearities, such as porosity-dependent shear viscosity and permeability within the iterative procedure (e.g., Räss, Duretz, & Podladchikov, 2019; Schmalholz et al., 2020; Wang et al., 2022). In our PT numerical algorithm, we use Equation 24 to calculate p_f , Equation 25 to calculate ϕ , Equation 26 to calculate p , and the two momentum balance Equation 27 to calculate v_x^s and v_y^s . The differential equations used to calculate ρ_s , X_s and D_{ij} are discretized with the same finite difference scheme and included inside the PT iteration loop so that they are continuously updated during the iterative solution of the five unknowns. The equations to determine τ_{ij} and σ_{ij} are also included in the PT iteration loop. Furthermore, the viscosities η_s and ζ are also continuously determined in the PT iteration loop due to their dependence on ϕ (Equations 16 or 17). Hence, the PT iteration loop fulfills two tasks at the same time: (a) the iterative calculation of the unknowns and (b) the iterative treatment of material nonlinearities for η_s and ζ , and for the ϕ -dependent effective permeability. All equations are solved within the same iteration loop and are updated iteratively with the current values of the physical quantities and material parameters. Therefore, after the convergence of the iterative solver, the numerical solution of the governing equations corresponds to a fully implicit numerical solution for a specific numerical time step (Räss et al., 2022). The fundamental features of the applied numerical algorithm and the iterative PT method are described in Appendix A1. Furthermore, we present a numerical resolution test and a numerical accuracy test of the applied numerical algorithm in Appendix A2.

3. Model Configuration, Characteristic Scales, and Dimensionless Parameters

3.1. Field Observations, Geodynamic Scenario, and Motivation for Model Configuration

In the Erro Tobbio region, the exhumed antigorite serpentinite exhibits locally metamorphic olivine veins (Figure 1) which indicates that the serpentinite has locally crossed the brucite-out reaction during subduction (Figure 2e). Before exhumation back to the surface, the antigorite serpentinite has never crossed the antigorite-out reaction, because this reaction would have generated peridotite (Figure 2e). Therefore, the olivine veins in the

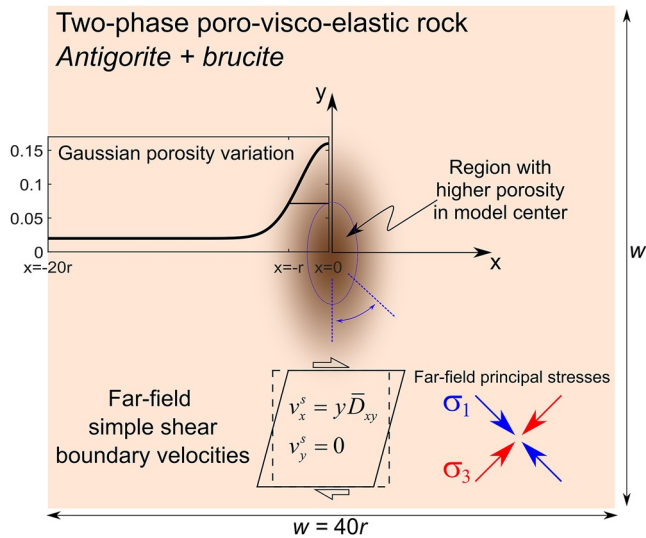


Figure 4. Sketch of the model configuration and the applied far-field simple shear (bottom sketch; see text for details). The initial distribution of the porosity is described by a 2D Gaussian distribution, having an initial horizontal bandwidth of $2r$ (graph in left middle of the sketch) and a vertical bandwidth of $4r$. The width, w , and height of the model is $40r$ and the applied far-field shearing rate is \overline{D}_{xy} . The orientations of the maximum and minimum principal stresses, σ_1 and σ_3 respectively, associated to the far-field simple shearing are indicated in the bottom right.

exhumed antigorite serpentinites have likely formed in a relatively narrow ambient pressure and temperature range (Figure 2e).

For our model, we assume that the antigorite serpentinite is sheared during subduction (Figure 2). For simplicity, the modeled serpentinite is made only of antigorite and brucite. We assume that the serpentinite is mechanically heterogeneous. Such heterogeneity is mimicked here by a spatially heterogeneous porosity, described further below, which causes a heterogeneous viscosity (Equations 16 and 17). The serpentinite includes small regions of higher porosity which generates small regions of lower viscosity. Such viscosity heterogeneities within a sheared viscous rock cause pressure variations around the regions with lower viscosity (e.g., Moulas & Schmalholz, 2020; Moulas et al., 2014; Schmid & Podladchikov, 2003). The pressure variations generate regions with smaller and higher pressure compared to the ambient pressure (e.g., Moulas et al., 2014). If pressure variations remain within the antigorite + brucite stability field and do not generate pressure below the reaction pressure, no metamorphic reactions occur in serpentinite (see potential prograde pressure-temperature path in Figure 3a). If the ambient pressure in the sheared serpentinite is close to the reaction pressure, then pressure variations can cause dehydration by generating pressures below the reaction pressure (Figure 2b). We are investigating dehydration reactions triggered by shearing-induced pressure variation in a scenario where ambient pressure is close to reaction pressure.

3.2. Model Geometry, Initial and Boundary Conditions

We consider a 2D quadratic model domain made of antigorite + brucite (Figure 4). We assume a constant temperature of 500°C for which the thermodynamic reaction pressure in our model is at 12.65 kbar (Figure 3). The exact temperature value is not essential for our study, because the variation of the solid and fluid densities with varying fluid pressure is similar for temperatures between 450 and 550°C (Figures 3a and 3b). We apply far-field simple shear for the boundary velocities (Figure 4). Shearing is parallel to the horizontal x -direction. The orientations of the maximum and minimum principal stresses, σ_1 and σ_3 respectively, associated with the far-field shearing are oriented at 45° to the shearing direction (Figure 4). We assume that p_f and p are initially identical and correspond to the ambient pressure, p_a . The ambient porosity, ϕ_a , is 2%, except in an elliptical region in the model center where the porosity exhibits a Gaussian distribution (Figure 4). The initial Gaussian distribution of the porosity is: $\phi_0 = \phi_a + A_\phi \exp[-(x/r)^2 - (y/2r)^2]$. A_ϕ is the amplitude of the initial porosity perturbation and the distance r controls the width, or variance, of the porosity distribution (Figure 4). We apply here an elliptical form of the Gaussian distribution with an initial axis ratio of 2 and with the long axis either parallel to the vertical y -direction or at 45° to the vertical direction (see the two blue dashed lines in Figure 4). The origin of the coordinate system is at the center of the elliptical region with positive coordinates indicating toward the right side and upwards (Figure 4). We will also present two simulations with a random initial perturbation of the porosity. The shear and bulk viscosities are smaller in the central region of the model due to the higher porosity. Boundary conditions for ϕ and p_f are of Dirichlet type, with boundary values fixed to the initial ambient values.

3.3. Compaction Length, Characteristic Time, and Dimensionless Numbers

In our simulations, we always consider the same dehydration reaction and its specific thermodynamic relation between fluid pressure and densities (Figure 3c). Hence, we present the results for pressures and densities in dimensional form with physical units. To conduct a specific numerical simulation, we need to specify various additional model parameters (Table 1). As long as they are within a realistic range for natural conditions, these additional parameters, such as ambient permeability, shear viscosities, far-field shearing rate, or size of the initial porosity perturbation, can be arbitrary. Furthermore, our numerical results are controlled by a set of independent dimensionless numbers (described further below) rather than by the values of each model parameter separately. We use such dimensionless numbers to describe and configure our numerical simulations because: (a) The set of

dimensionless numbers represents the smallest possible number of parameters to specify a numerical simulation. (b) The dimensionless numbers help select the most suitable model parameters for simulating dehydration veins (see further below). (c) The numerical results obtained from a single simulation can be scaled to a wide range of realistic dimensional parameters using dimensionless numbers, making them more general. We present such scaling in the Discussion section.

The dimensionless numbers involve a characteristic length scale, δ , and a characteristic time scale, t_c . In a viscously deformable porous medium, the compaction of the poro-viscous medium and associated spatial variations in solid and fluid velocities occur over a characteristic length scale which is termed the compaction length (e.g., McKenzie, 1984). We use this compaction length as δ . Similarly, the compaction and associated porous fluid flow occurs over a characteristic hydraulic diffusion time scale, which we use as t_c . The δ and t_c are given by:

$$\delta = \sqrt{\frac{k\phi^3}{\eta_f} \left(\zeta(\phi) + \frac{4}{3}\eta_s(\phi) \right)} \quad (28)$$

$$t_c = r^2 \eta_f / (k \phi^3 K_s)$$

In our model with porosity-dependent effective permeability, and porosity-dependent shear and compaction viscosities, both δ and t_c depend on ϕ . The set of applied dimensionless numbers is:

$$\Omega_1 = \frac{\delta}{r} \Big|_{\phi=\phi_a}, \quad \Omega_2 = \frac{\overline{D}_{xy}\eta_s}{p_a} \Big|_{\phi=\phi_a}, \quad \Omega_3 = \frac{w}{r},$$

$$\Omega_4 = \frac{\zeta}{\eta_s} \Big|_{\phi=\phi_a}, \quad \Omega_5 = \frac{t_{kin}}{t_c} \Big|_{\phi=\phi_a}, \quad \Omega_6 = \frac{t_{Max}}{t_c} \Big|_{\phi=\phi_a}, \quad (29)$$

where w is the model width and \overline{D}_{xy} is the applied far-field simple shear rate (Figure 4). All dimensionless numbers that are dependent on the porosity are evaluated for the applied ambient porosity, $\phi_a = 2\%$. Ω_1 represents the dimensionless δ that is normalized by r . Ω_2 determines the magnitude of the shear stress resulting from the applied far-field simple shear compared to the ambient pressure p_a . Ω_3 indicates the size difference between the model domain and r . Ω_4 indicates the magnitude of ζ compared to η_s . Ω_5 scales the kinetic time to the hydraulic diffusion time. Ω_6 scales the Maxwell time to the hydraulic diffusion time.

3.4. Configuration of the Reference Simulation S1

We configure one reference simulation, termed S1, and configure 20 additional simulations, S2 to S21, to test the impact of various features on the simulations. The parameters applied for the simulations are listed in Table 2.

Ω_1 is a crucial parameter for the model configuration because deformation associated with compaction occurs over a distance that is several times larger than δ (e.g., McKenzie, 1984). For $\Omega_1 \ll 0.01$, compaction occurs over a distance much smaller than the initial porosity distribution, and it is unfeasible to numerically resolve both the porosity perturbation and the compaction since they occur on significantly different length scales. On the other hand, for $\Omega_2 \gg 0.1$, compaction occurs on a spatial scale larger or equal to the size of the porosity perturbation and it is difficult to generate significant fluid pressure perturbations within small areas around the weak region with increased porosity. Values for Ω_1 that are in the range between 0.01 and 0.1 are, therefore, often used in simulations of porosity waves (e.g., Dohmen & Schmeling, 2021; Simpson & Spiegelman, 2011). Hence, we apply $\Omega_1 = 0.033$ for our reference simulation (Table 2). For S1, we apply $\Omega_2 = 0.11$ so that the shear stress resulting from the applied far-field simple shear is approximately one order of magnitude smaller than the ambient pressure. We apply $\Omega_3 = 40$ so that the model domain is significantly larger than the applied porosity perturbation. We use $\Omega_4 = 2$ what is supported by theoretical models and experiments (e.g., Katz et al., 2022; Yarushina & Podladchikov, 2015), and we apply $\Omega_5 = 0.0025$ so that the kinetic time scale is significantly faster than the hydraulic diffusion time scale. We further use $\Omega_6 = 0.001$ so that the visco-elastic time scale and the associated time for visco-elastic stress buildup is significantly faster than the hydraulic diffusion time.

To configure S1, we must further specify the relationships between η_s and ϕ , and between η_s and ζ . For S1, we apply an exponential dependence of η_s on ϕ , and we use $a = 1/2.5$ (Equation 16; Figure 5a). The considered variation of η_s , normalized by the viscosity for the ambient porosity, η_{sa} , with increasing ϕ is displayed in Figure 5a. For comparison, we illustrate representative values for experimentally determined shear viscosities for partially

Table 2
Parameters for Performed Simulations

Simulation	p_a [kbar]	Ω_1	Ω_2	Ω_3	Ω_4	Ω_5	Ω_6	$\zeta \propto 1/\phi$	a	Compaction
S1*	12.75	0.033	0.11	40	2	0.0025	0.001	No	1/2.5	visco-elastic
S2								Higher ambient pressure: $p_a = 14.5$ [kbar]		
S3								Higher ambient pressure: $p_a = 13.5$ [kbar]		
S4								Smaller dimensionless compaction length: $\Omega_1 = 0.012$		
S5								Larger dimensionless compaction length: $\Omega_1 = 0.052$		
S6								Larger dimensionless compaction length: $\Omega_1 = 0.082$		
S7								Larger dimensionless compaction length: $\Omega_1 = 0.33$		
S8								Shear viscosity is a power-law function of porosity: $n = 4$		
S9								Shear viscosity is a power-law function of porosity: $n = 3$		
S10								Shear viscosity is a power-law function of porosity: $n = 2$		
S11								Plastic yield stress: $\tau_y = 100$ [MPa]		
S12								Initial porosity perturbation has vertical orientation		
S13								Initial porosity perturbation has vertical orientation AND plastic yield stress: $\tau_y = 100$ [MPa]		
S14								Initial random porosity perturbation AND $\tau_y = 100$ [MPa]		
S15								Viscous compaction only		
S16								Compaction viscosity depends on $1/\phi$		
S17								Compaction viscosity depends on $1/\phi$ AND $\Omega_4 = 20$		
S18								Faster kinetics: $\Omega_5 = 2.5 \times 10^{-4}$		
S19								Faster kinetics: $\Omega_5 = 2.5 \times 10^{-5}$		
S20								$p_a = 14.5$ [kbar] AND $\Omega_1 = 0.33$		
S21								Initial random porosity perturbation AND $p_a = 14.5$ [kbar] AND $\Omega_1 = 0.33$		

Note. All parameters for the reference simulation S1 are given. For the additional simulations S2 to S21, only the parameters that are different compared to S1 are given. *S1 has further: $\alpha = 0.5$, no plastic yield stress, and oblique orientation of initial porosity perturbation.

molten rock as a function of porosity (experimental data is taken from the compilation of Katz et al. (2022); see figure caption for all references). The effective shear viscosity of a porous medium can vary by 3–4 orders of magnitude with a change in porosity from 2% to 25% according to experimental data. For S1, we do not consider the dependence of ζ on $1/\phi$, Equation 20, and only apply the relation $\zeta = \Omega_4 \eta_s$. The $1/\phi$ dependence of ζ is evaluated in two additional simulations. After specifying the relations between η_s , ζ and ϕ we can plot the relation between δ/r and ϕ (Figure 5b). With increasing ϕ , values of δ/r first increase and then decrease (Figure 5b). The maximum value of δ/r is approximately 25 times larger than the minimum value of δ/r (Figure 5b). We apply an amplitude of the initial Gaussian ϕ perturbation of $A_\phi = 12$ so that the maximum ϕ in the model center is 24%. For the applied relation between η_s on ϕ , the minimum initial η_s in the model center is then approximately 100 times smaller than η_{sa} (Figure 5a). The long axis of the initial Gaussian ϕ distribution is oriented 45° concerning the vertical y -direction so that the long axis is parallel to the maximum principal stress for the applied far-field simple shear (σ_1 in Figure 4). We apply for S1 an ambient pressure $p_a = 12.75$ kbar that is close to the reaction pressure $p_r = 12.65$ kbar (Figures 3c and 3d). Finally, for S1 and for all additional simulations, we apply a value of 3 for the porosity exponent in the effective permeability, Equation 11 (e.g., Katz et al., 2022; Malvoisin et al., 2015), and we apply $K_d/K_s = 0.5$ so that $\alpha = 0.5$, termed often the Biot-Willis coefficient, Equation 19, which is a representative value for porous rock (e.g., Hofmann et al., 2005).

3.5. Applied Parameters for Additional Numerical Simulations

To test the impact of various parameters on the results of S1 we performed 20 additional simulations (Table 2). To evaluate the impact of p_a on the results we perform two additional simulations, S2 and S3 (Table 2), with higher values of p_a . To test the impact of Ω_1 on the simulation results we perform four simulations with different Ω_1 for

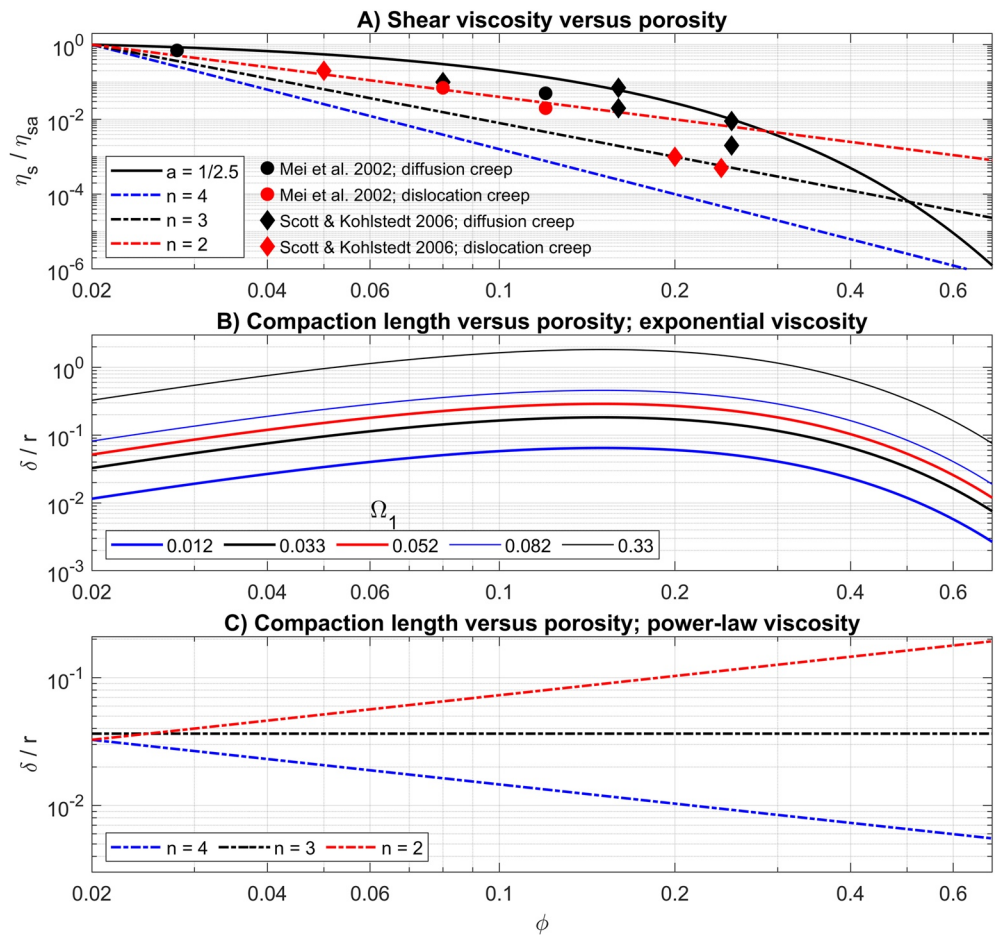


Figure 5. Shear viscosity and compaction length vs. porosity. (a) Applied values of η_s , normalized by the shear viscosity for the ambient porosity, η_{sa} , versus ϕ . Diamonds and circles indicate representative experimental data for the shear viscosities of partially molten rocks (data taken from the compilation in Katz et al. (2022), their Figure 2b, with original references given in the legend) (Scott & Kohlstedt, 2006). (b) Curves of normalized compaction length, δ/r , versus ϕ for shear viscosities, η_s , that are an exponential function of ϕ . The parameter a is always $1/2.5$ (see Equation 16). (c) Curves of δ/r versus ϕ for η_s that are a power-law function of ϕ . The applied power-law exponents, n , are indicated in the legend (see Equation 17).

the same relation between η_s and ϕ (Figure 5b; simulations S4 to S7 in Table 2). We also perform three simulations for η_s with a power-law dependence on ϕ (Equation 17). We use three values for the power-law exponent, namely $n = 2, 3,$ and 4 (Figures 5a and 5c), to obtain values of δ/r that are increasing, constant or decreasing, respectively, with increasing ϕ (Figure 5b; S8 to S10 in Table 2). For all three δ/r versus ϕ relations the values of $\Omega_1 \approx 0.035$ (Figure 5b). In S11 we apply a plastic yield stress $\tau_y = 100$ MPa. To evaluate the orientation of the initial porosity perturbation we perform S12 in which the long axis of the porosity perturbation is vertical and S13 which has additional $\tau_y = 100$ MPa (Table 2). To test the impact of a more realistic initial porosity distribution, we perform S14 that has an initial random porosity distribution and $\tau_y = 100$ MPa. S15 is identical to S1 except that we consider viscous compaction only by setting the term multiplied by $1/K_d$ in Equation 19 to zero, that means $K_d = \infty$. In S16 and S17 we consider again visco-elastic compaction and consider the dependence of ζ on $1/\phi$ (Equation 20). In S17, we apply additionally $\Omega_4 = 20$ which means that ζ is an order of magnitude larger than η_s compared to S1. We also test the impact of the kinetic time scale and perform simulations S18 and S19 with a kinetic time scale that is one and two orders of magnitude faster, respectively, compared to S1. Finally, we perform S20 and S21 with a high ambient pressure $p_a = 14.5$ kbar and a larger compaction length $\Omega_1 = 0.33$ compared to S1 to evaluate simulations for conditions that are not suitable to trigger dehydration and significant pressure perturbations.

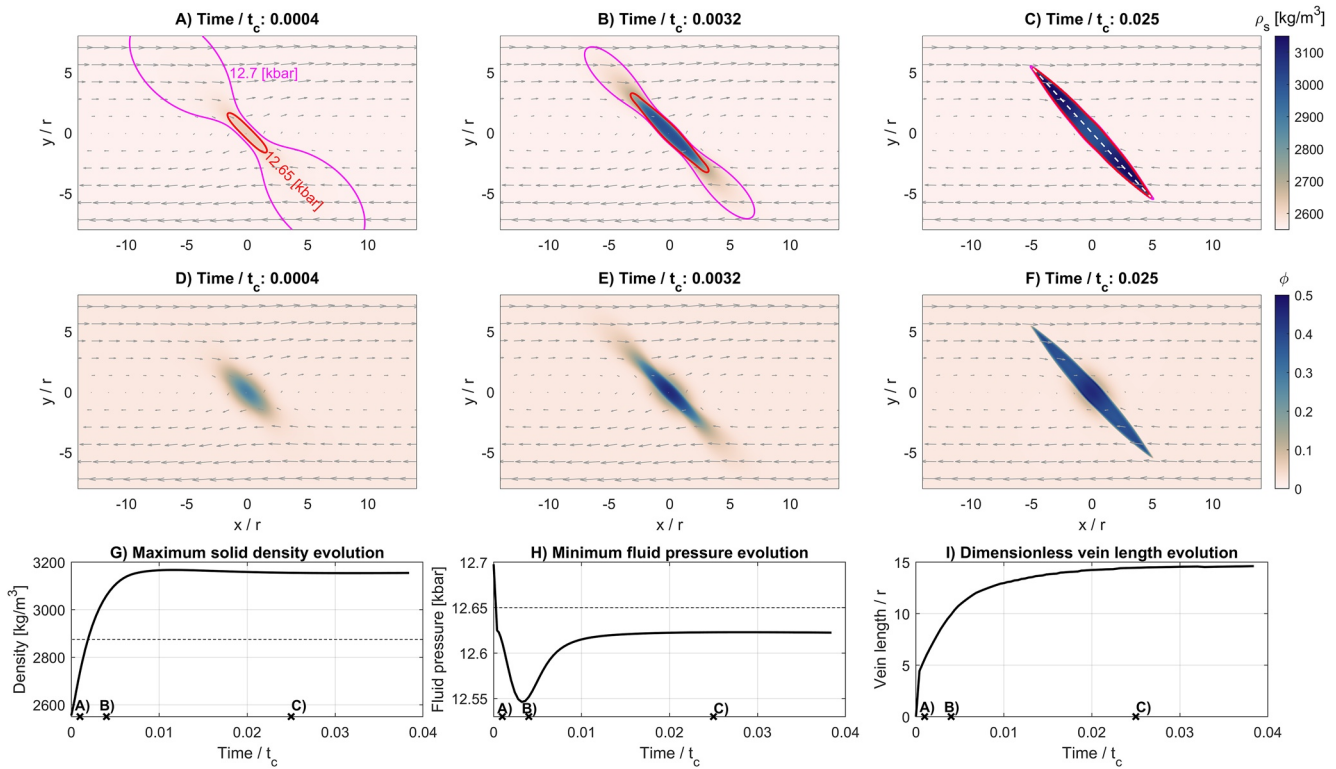


Figure 6. The reference simulation S1 (see Table 2). Panels (a–c) show color plots of solid density, ρ_s , at three different dimensionless model times. Time is normalized by t_c for the ambient porosity (Equation 28). Additionally, two contour lines of the fluid pressure, p_f , are indicated. Panels (d–f) show color plots of the porosity, ϕ , at the same three dimensionless model times as in (a–c). (g) Evolution of the maximum solid density for each numerical time step vs. the dimensionless model time. The model times corresponding to the three model times displayed in (a–c) are indicated on the horizontal axis. (h) Evolution of the minimum fluid pressure for each numerical time step vs. the dimensionless model time. (i) Evolution of the dimensionless vein length, normalized by r , vs. the dimensionless model time. The contour for $p_f = 12.65$ kbar has a form like an ellipse and the vein length corresponds to the long axis of this ellipse. For clarity, the vein length is indicated with the white dashed line in panel (c).

4. Results

4.1. Overview

The result section is structured in two general parts. In the first part, we investigate the evolution of the reference simulation S1 and the main differences of simulations S2 to S19 compared to S1. In the second part, we focus on S1 to quantify the mechanisms which cause the generation and evolution of porosity during shearing and dehydration. Simulations S20 and S21 are discussed in the Discussion section.

In the figures, dimensional quantities are displayed with their physical units in square braces, such as ρ_s [kg/m³]. The horizontal, x , and vertical, y , coordinates are normalized by r and the simulation time as well as all displayed rates, for example, $\nabla \cdot \mathbf{v}^s$, are normalized by t_c , whereby t_c is calculated for the ambient porosity, ϕ_a . Dimensionless ratios are presented without any indication of units, such as x/r .

4.2. The Reference Simulation S1

The two quantities ρ_s and p_f can vary in space and time in our model. They also appear in both the thermodynamic relations (Figure 3) and the equations governing the hydromechanical behavior, like Equations 24–26. We, therefore, described first the evolution of ρ_s and p_f for S1. During the initial stages of S1 an elongated region with $p_f < 12.7$ kbar develops and inside this region is a smaller, elliptical region with $p_f < 12.65$ kbar (Figure 6a). Changes of ρ_s due to dehydration start when $p_f < 12.7$ kbar because the dehydration reaction in our model occurs over a pressure interval of 0.1 kbar (Figure 3c). Values of ρ_s are slightly increased within the region bound by the contour line for $p_f = 12.65$ kbar, indicating the onset of dehydration and the reaction from antigorite + brucite to forsterite (Figure 6a). With progressive shearing the region with $p_f < 12.7$ kbar becomes smaller and the one

with $p_f < 12.65$ kbar larger (Figures 6b and 6c). At the end of the simulation both contour lines for $p_f = 12.7$ and 12.65 kbar are essentially identical (Figure 6c). Values of ρ_s inside these contours have significantly increased to values $> 3,100$ kg/m³, indicating the formation of an olivine vein (Figure 6c). The increase of ρ_s and the dehydration cause an increase of ϕ (Figures 6d–6f). The region with increasing ρ_s corresponds to the region with increasing ϕ during progressive shearing (Figures 6d–6f). The maximum values of ϕ are approximately 0.5, also in regions where ϕ_0 was 0.02. In these regions, the porosity increased, hence, by a factor of 25 during dehydration.

A plot of the maximum value of ρ_s versus the progressive dimensionless time shows that ρ_s first significantly increases and then eventually reaches a constant value (Figure 6g). The presented maximum values correspond to the maximum values in the entire model domain at one numerical time step. The minimum value of p_f in the model domain first decreases to a value of ~ 12.55 kbar, then increases to a value of ~ 12.62 kbar and then also reaches a constant value. To quantify the growth of the dehydration region we measure the maximum straight distance inside the closed contour line for $p_f = 12.65$ kbar. The contour for $p_f = 12.65$ kbar has a form like an ellipse and the measured distance corresponds, hence, to the long axis of this ellipse (white dashed line in Figure 6c). We refer to region inside the contour for $p_f = 12.65$ kbar as dehydration vein and to the length of its long axis as vein length (Figure 6i). The vein length grows fastest during the initial stages of the simulation and then progressively slows down until the vein length reaches a constant value (Figure 6i). The vein grows in the direction parallel to the maximum principal stress imposed by the far-field shearing (σ_1 direction in Figure 4).

S1 shows that dehydration vein growth is a self-limiting process in our model because the vein stops growing once the minimum value of p_f stops changing. Concerning the testing of the process hypothesis for olivine vein growth due to shear-driven dehydration, S1 shows that the mechanisms and process proposed in the hypothesis are physically feasible in the sense that they can be predicted with a 2D HMC model. From an algorithmic point of view, S1 shows that the newly developed numerical HMC algorithm can capture the significant density and porosity variations caused by the spontaneous formation of serpentinite dehydration.

4.3. Impact of Ambient Pressure on Dehydration Vein Formation, S2 and S3

Simulations S2 and S3 are identical to S1 except that $p_a = 14.5$ and 13.5 kbar, respectively (Table 2). For S2, p_f does not decrease below 12.7 kbar in the model domain (Figures 7a–7d). During significant simple shearing, the initial ϕ perturbation is sheared and rotated (see red porosity contours in Figures 7a–7d) and p_f perturbations are always present around the region with higher ϕ (Figures 7a–7d). No vein-like structure with increased ϕ , oriented parallel to σ_1 , develops in the model when no dehydration reaction takes place. For S3, p_f decreases locally below 12.7 kbar after some shearing (black contour lines in Figures 7f–7h) and two separate, elongated regions with decreased p_f and increased ϕ develop (Figures 7f–7h). ϕ in these regions is increased with respect to ϕ_a (change of red contour line in Figures 7e–7h). However, no single continuous, vein-like region develops (Figure 7h). For comparison, we show the evolution of the same quantities for S1. For S1, a single elongated region with $p_f < 12.7$ kbar develops in which ϕ is increased with respect to ϕ_a (Figures 7i–7l). The results show that if no dehydration reaction takes place, no elongated, or vein-like, region with increased ϕ develops. Also, for the applied model configuration, p_a of 13.5 kbar is sufficiently close to the reaction pressure of 12.65 kbar so that shear-driven perturbations in p_f can trigger dehydration (Figure 7).

4.4. Impact of Compaction Length, S4, S7 to S10

S4 and S7 are identical to S1 (with $\Omega_1 = 0.033$) except that $\Omega_1 = 0.012$ and 0.33, respectively (Table 2; results of S5 and S6 will be presented in Figure 12). For S4, two elongated, separate regions with $\rho_s > 3,100$ kg/m³ develop during shearing, indicating the reaction from serpentinite to olivine (Figures 8a–8d). S4 was run until it failed to converge, which was caused by extremely sharp spatial gradients in material properties and deformation around the two vein tips. The sharp gradients are related to the applied value of Ω_1 , resulting in a compaction length approximately three times shorter than for S1. This causes sharper deformation gradients on a smaller length scale. For comparison, for S1 one continuous elongated region with $\rho_s > 3,100$ kg/m³ develops (Figures 8e–8h), showing the formation of an olivine vein. For S7 with $\Omega_1 = 0.33$, also one continuous elongated region with increased values of ρ_s develops, but maximum values of ρ_s only reach approximately 2,940 kg/m³ (Figures 8i–8l).

With S8 to S10 we test the impact of a power-law dependence of η_s on ϕ , Equation 17, and the correspondingly different relation between δ/r and ϕ (Figures 5a and 5c). For S8, the power-law exponent $n = 4$ and values of δ/r

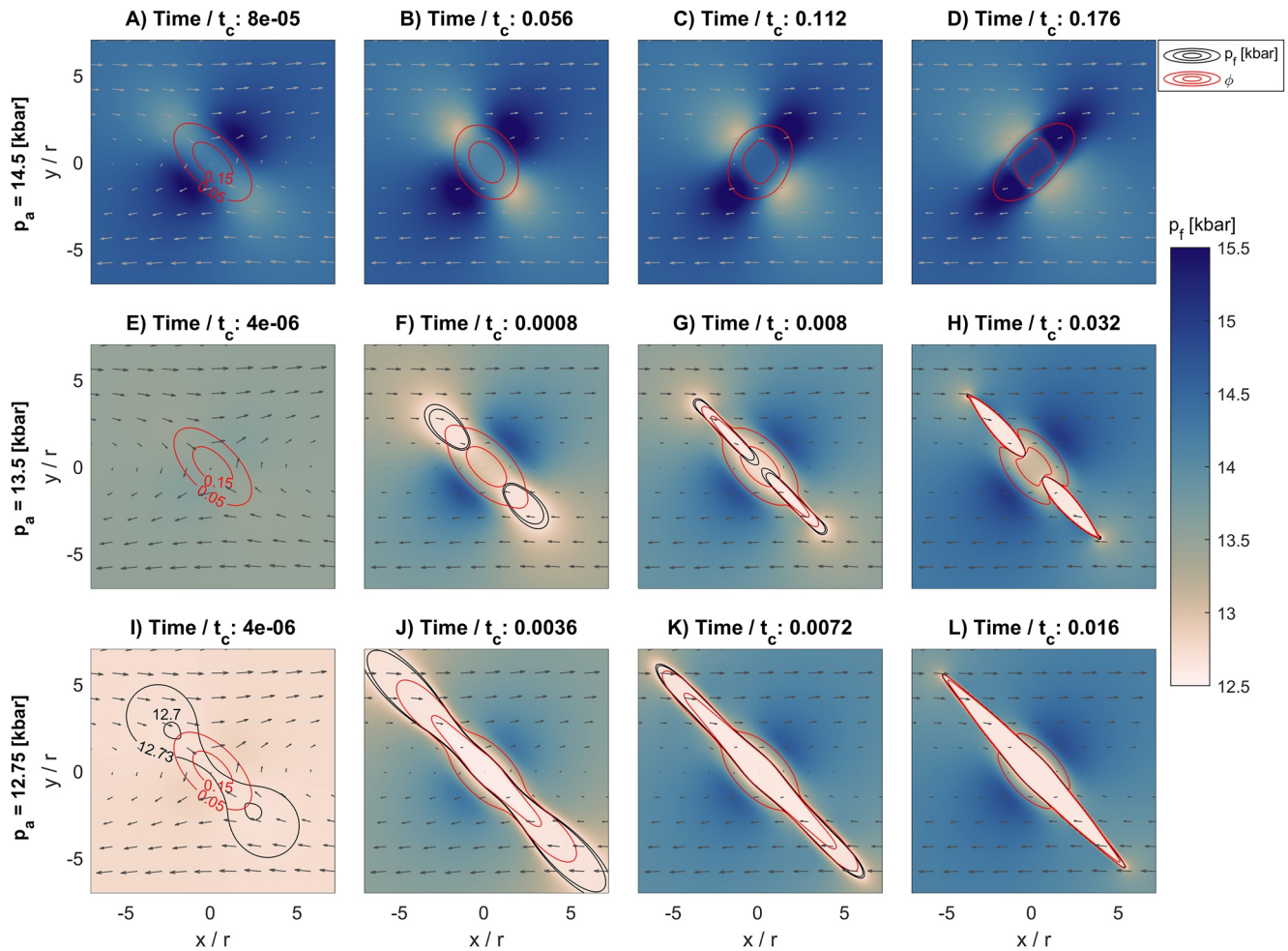


Figure 7. Color plots showing the evolution of fluid pressure, p_f , with progressive simple shearing for three values of the ambient pressure, p_a . Time displayed in panels is dimensionless and normalized by t_c for the ambient porosity (Equation 28). Panels (a–d) show results of simulation S2 for p_a of 14.5 kbar, (e–h) of S3 for p_a of 13.5 kbar and (i–l) of S1 for p_a of 12.75 kbar. Red contours indicate porosity, ϕ , and black contours p_f (see legend). For better comparison, the color scale is the same for all panels. Applied parameters in the simulations are given in Table 2.

monotonously decrease with increasing ϕ (Figure 5c). In S8, an elongated region with increased ρ_s and decreased p_f develops (Figures 9a–9d). However, S8 generates maximum values of only $\rho_s = 2,765 \text{ kg/m}^3$ and no finite region develops that is bounded everywhere by sharp gradients in ρ_s , like in S1 (Figure 8h). In contrast, the region with increased values of ρ_s continuously grows until it reaches the model boundaries. For S9, $n = 3$ and values of δ/r are constant with increasing ϕ . Like in S8, an elongated region with increased ρ_s and decreased p_f develops (Figures 9e–9h). Maximum values of ρ_s only reach values of $2,865 \text{ kg/m}^3$. A region with increased values of ρ_s continuously grows until it reaches the model boundaries, like for S8. For S10, $n = 2$ and values of δ/r monotonously increase with increasing ϕ (Figure 5c). Maximum values of ρ_s reach $3,015 \text{ kg/m}^3$, but like in S8 and S9 the region with increased ρ_s always grows until the model boundaries and it exhibits strong gradients of ρ_s . Hence, in contrast to S1, no olivine veins of finite size, with homogeneous values of ρ_s and with $\rho_s > 3,100 \text{ kg/m}^3$ form in S8 to S10. Therefore, an exponential relation between η_s and ϕ is more suitable to form olivine dehydration veins compared to a power-law relation. Such an exponential relation is also typically used in melt migration studies (e.g., Katz et al., 2006; Schmeling et al., 2012) and supported by laboratory experiments (Figure 5a).

4.5. Impact of Plasticity and Initial Porosity Perturbation, S11 to S14

In regions with constant ϕ , η_s is also constant and the modeled poro-viscous medium flows like a linear viscous fluid. To test the impact of significant nonlinear flow, we apply a pressure-insensitive yield stress, τ_y ,

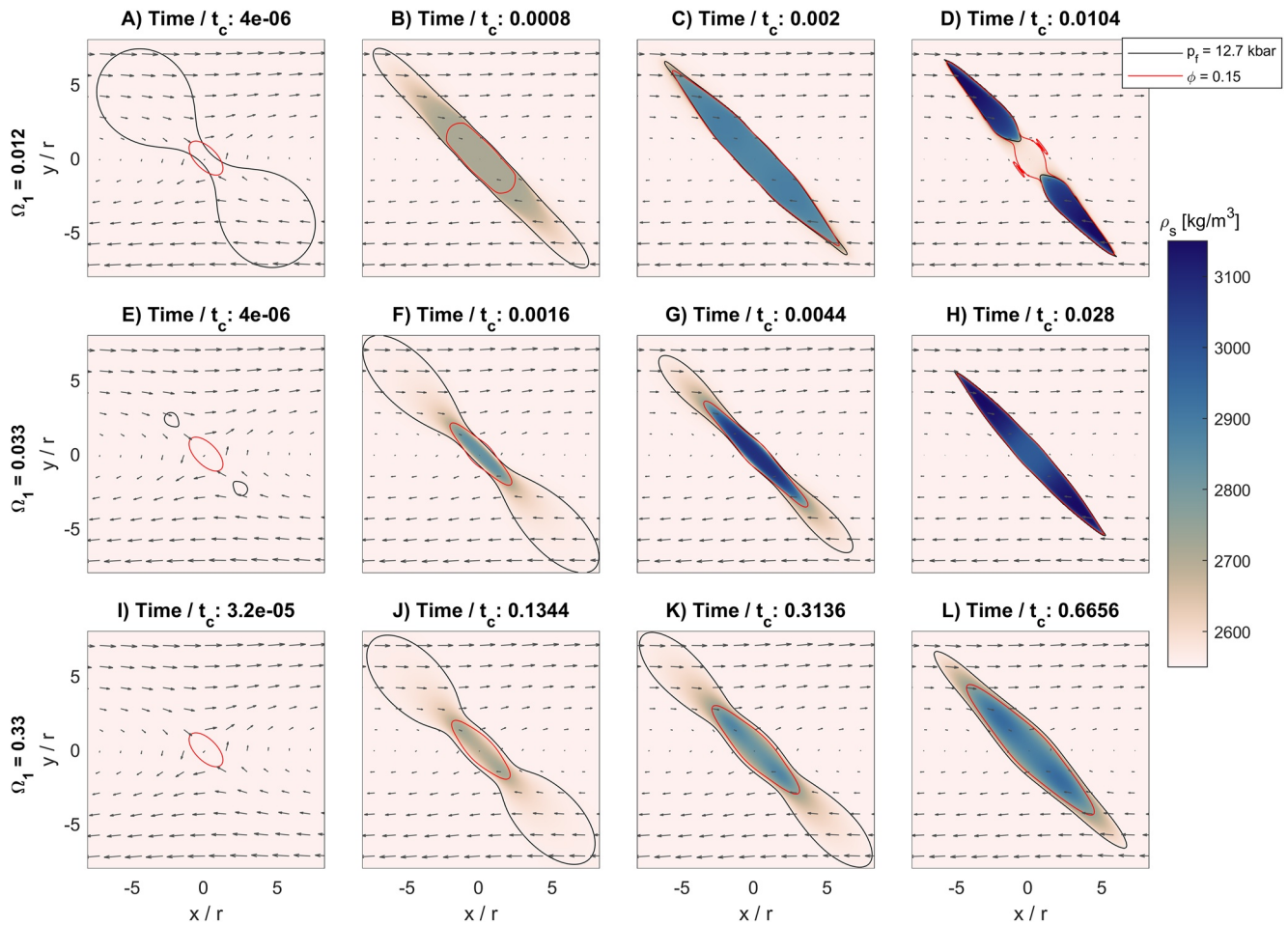


Figure 8. Color plots showing the evolution of solid density, ρ_s , with progressive simple shearing for simulations S4 (a–d), S1 (e–h) and S7 (i–l) having different values of Ω_1 that are indicated to the left of each row of subplots. Applied model parameters are given in Table 2. The shear viscosity has an exponential dependence on porosity (Figure 5a). Time displayed in panels is dimensionless and normalized by t_c for the ambient porosity (Equation 28). Red contours indicate porosity, ϕ , of 0.15 and black contours indicate fluid pressure, p_f , at 12.7 kbar (see legend).

corresponding to a von Mises type yield criterion (Equation 18). S11 is identical to S1 except the application of a yield stress $\tau_y = 100$ MPa (Figures 10a–10d). Without application of τ_y , the maximum deviatoric stresses in S1 are approximately 150 MPa. Overall, S11 evolves similarly to S1, but with shorter vein length (Figures 10a–10d). The application of a yield stress, τ_y , and the associated nonlinear viscous flow, or creep, does, hence, not significantly impact the formation of olivine veins.

In S12 we rotate the initial orientation of ϕ by 45° so that the long axis of the elliptical ϕ perturbation is vertical (Figures 4 and 10e); all other parameters are identical compared to S1. Like for S1, for S12 a vein-like region with $\rho_s > 3,100$ kg/m³ forms and grows in direction to the maximum compressive principal stress (Figures 10e–10h). S13 is identical to S12 but with the application of $\tau_y = 100$ MPa (Figures 10i–10l). The application of τ_y does also not significantly impact the olivine vein formation but causes a shorter vein length, like in S11.

In S14, we apply initially a random ϕ perturbation and $\tau_y = 100$ MPa to test whether olivine veins also develop for more realistic ϕ perturbations and nonlinear creep (Figure 11). We generated the initial ϕ distribution with the random field generator presented in Räss, Kolyukhin, and Minakov (2019). With progressive shearing, several vein-like regions with $\rho_s > 3,100$ kg/m³ (Figures 11a–11d) and $\phi > 0.4$ (Figures 11e–11h) develop. The long axes of these veins are oriented parallel to σ_1 and the veins have in several regions an en échelon arrangement. The values of τ_{II} are smallest inside the veins due to the low, porosity-dependent η_s . Due to this porosity dependence of η_s , the magnitudes of τ_{II} are very heterogeneous throughout the model (Figures 11i–11l). The area-averaged value of τ_{II} in the model for each time step is a proxy for the area-averaged shear strength and effective viscosity

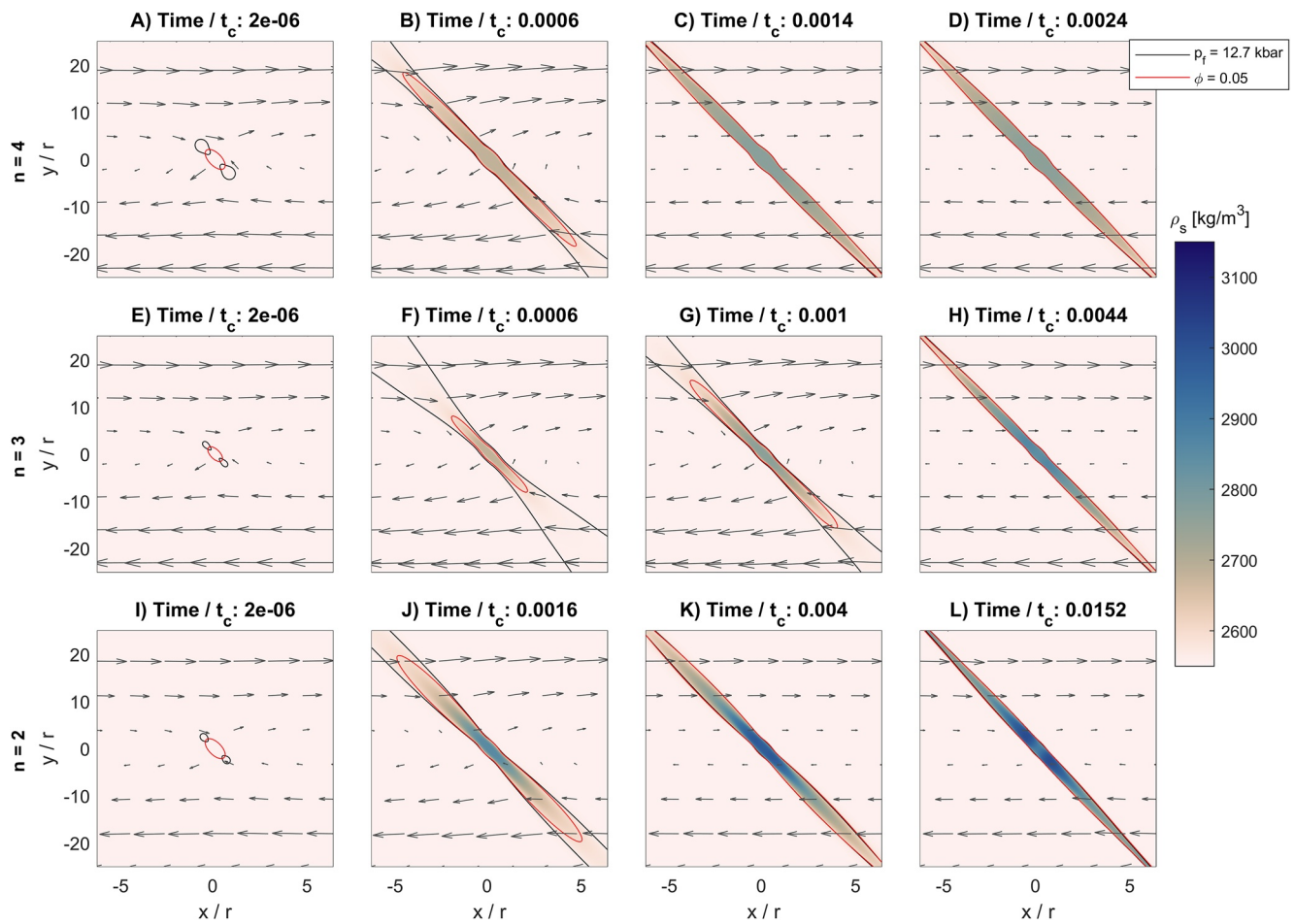


Figure 9. Color plots showing the evolution of solid density, ρ_s , with progressive simple shearing for a shear viscosity with power-law dependence on porosity (Figure 5a). Results are displayed for simulations S8 (a–d), S9 (e–h), and S10 (i–l) having different values of the power-law exponent, n , that are indicated to the left of each row of subplots. Applied model parameters are given in Table 2. Time displayed in panels is dimensionless and normalized by t_c for the ambient porosity (Equation 28). Red contours indicate porosity, ϕ , of 0.05 and black contours indicate fluid pressure, p_f , at 12.7 kbar (see legend).

of the model domain, if a constant far-field shearing rate is applied, as done here. The increase of the areas with smaller τ_{II} with progressive shearing (Figures 11i–11l) indicates, hence, a decrease of the average viscosity and, consequently, a weakening of the rock unit represented by the model domain.

In summary, the simulations S11 to S14 with different initial ϕ perturbations and nonlinear creep, modeled here in a simple way by the application of τ_y , show that the geometry of the initial ϕ perturbation and the type of flow law for the solid deformation do not significantly impact the dehydration and olivine vein formation. Also, olivine veins are formed in our model for more realistic model configurations considering random initial ϕ perturbations.

4.6. Impact of Compaction Viscosity, S15 to S17, and Kinetics, S18 and S19

We show the results of S15 to S19 in a single figure due to their similar evolution to S1 (Figure 12). For completeness, we also show results for S5 ($\Omega_1 = 0.052$) and S6 ($\Omega_1 = 0.082$). We show the temporal evolution of maximum values of ρ_s , of minimum values of p_f and of the vein length (Figure 12). All simulations show only small to moderate differences in the final vein length (Figure 12a), but the same final values for minimum p_f and maximum ρ_s (Figures 12b and 12c). The results for S15 with viscous compaction are like the results for S1 indicating that the elastic component of the visco-elastic compaction has a minor impact for the considered model. In S16, ζ depends on $1/\phi$. The final vein length is slightly larger compared to S1 (Figure 12a), the minimum p_f of the entire simulation is a bit smaller compared to S1 and reached earlier (Figure 12b), whereas the evolution of maximum ρ_s is like in S1 (Figure 12c). In S17, ζ depends also on $1/\phi$

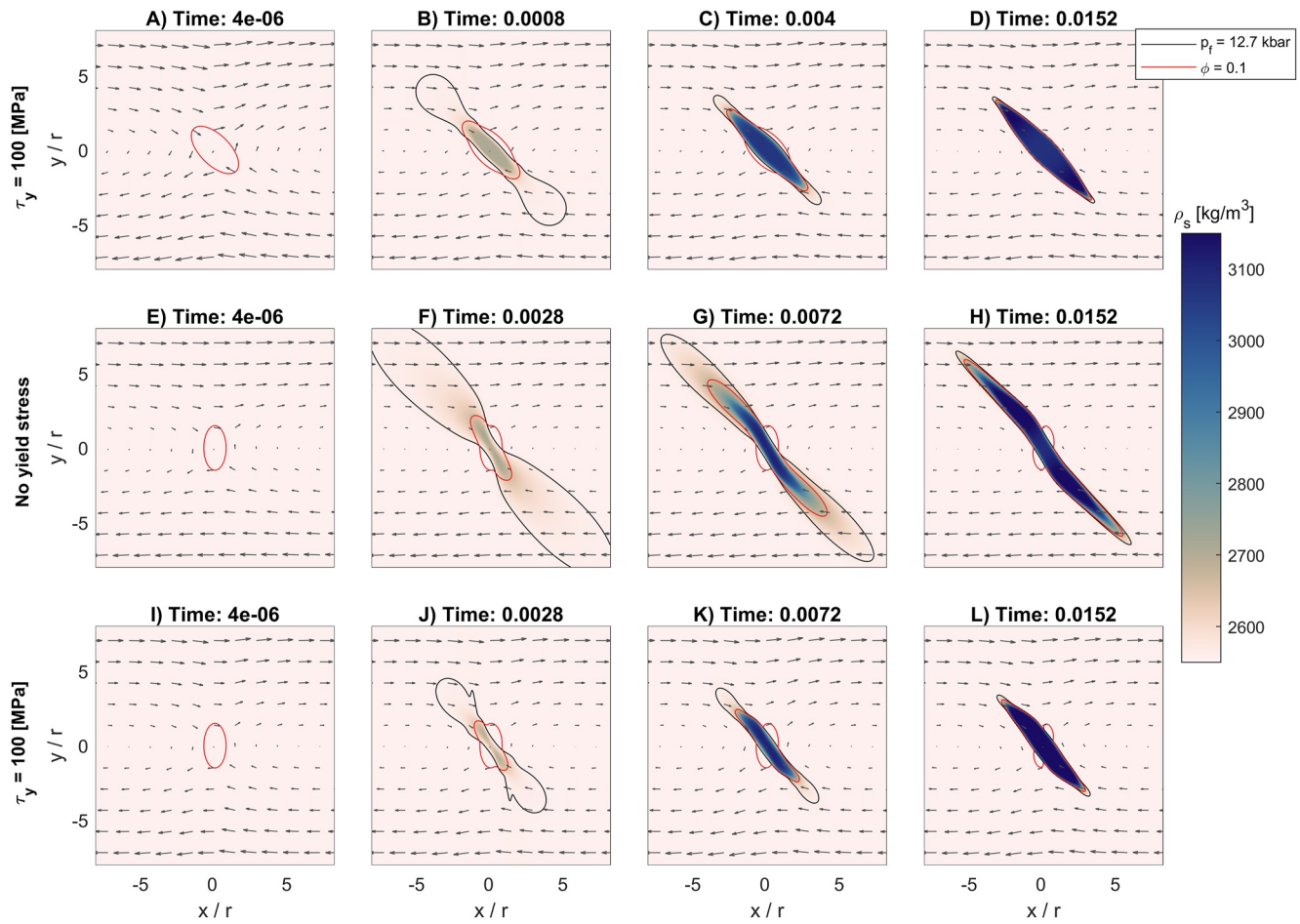


Figure 10. Color plots showing the evolution of solid density, ρ_s , with progressive simple shearing for simulations S11 (a–d), S12 (e–h), and S13 (i–l). S11 and S13 consider a yield stress, indicated to the left of each row of subplots, and S12 and S13 have an initial porosity perturbation that is rotated 45° compared to S11 (see red contours in panels (a, e, and i)). Applied model parameters are given in Table 2. The shear viscosity has an exponential dependence on porosity (Figure 5a). Time displayed in panels is dimensionless and normalized by t_c for the ambient porosity (Equation 28). Red contours indicate porosity, ϕ , of 0.1 and black contours indicate fluid pressure, p_f , at 12.7 kbar (see legend).

and by applying $\Omega_4 = 20$ we additionally made ζ one order of magnitude larger compared to S1. For S17, the final vein length is slightly shorter compared to S1 (Figure 12a), the minimum p_f of the entire simulation is also a bit smaller compared to S1 but reached later (Figure 12b), and the evolution of maximum ρ_s is again like in S1 (Figure 12c). S16 and S17 show that the dependence of ζ on $1/\phi$ and the initial magnitude of ζ do not significantly impact the formation of olivine veins caused by dehydration, at least for the parameter range considered here.

In S18 and S19 we decreased the kinetic time, t_{kin} , by one and two orders of magnitude, respectively, compared to S1. Results of S19 are like results of S18 indicating that S19 represents the case of infinitely fast kinetics because reducing t_{kin} even more would not change the results considerably. S19 represents, hence, a simulation with negligible reaction kinetics. Due to the significantly faster kinetics, maximum ρ_s grow faster compared to S1 (Figure 12c). This faster density change causes faster dehydration and associated faster volume increase which in turn increases p_f compared to S1. Therefore, S18 and S19 show a higher minimum p_f compared to S1 and the minimum p_f decreases below 12.65 kbar later compared to S1 (Figure 12b). Therefore, also the vein growth starts later in S18 and S19 compared to S1 (Figure 12a).

S5 and S6 have intermediate compaction lengths between the ones of S1 and S7. In S5 and S6 the Ω_1 is larger compared to S1 and, hence, the growth of the vein length and of maximum ρ_s is significantly slower. Nevertheless, in both S5 and S6 the minimum p_f and the maximum ρ_s reach the same final values as all other simulations.

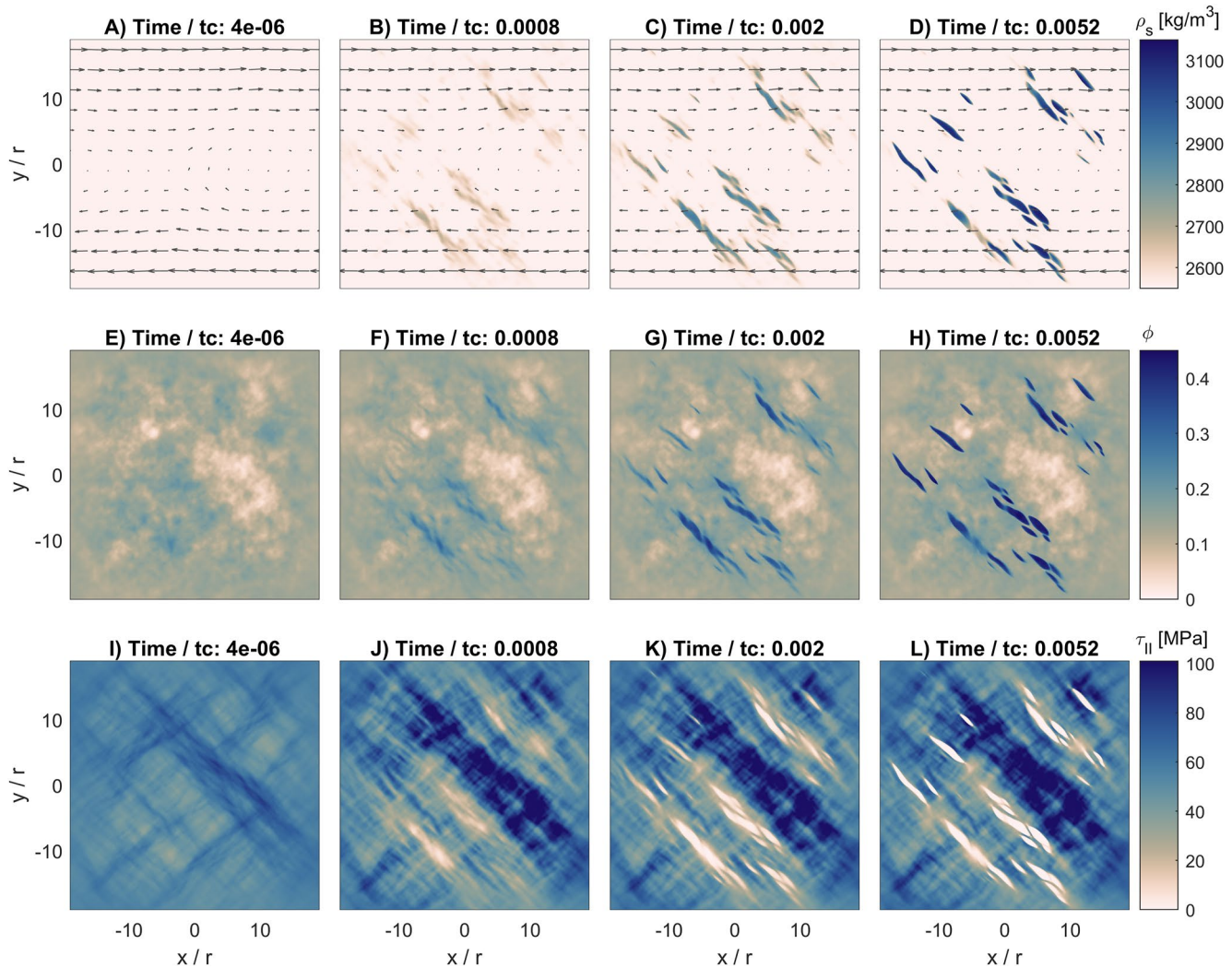


Figure 11. Results for simulation S14 with an initial random porosity distribution and a yield stress of 100 MPa. Applied model parameters are given in Table 2. Panels (a–d) shows time evolution of solid density, (e–h) of porosity and (i–l) of the square root of the second invariant of the deviatoric stress tensor, $\tau_{II} = \sqrt{0.5(\tau_{xx}^2 + \tau_{yy}^2) + \tau_{xy}^2}$. Time displayed in panels is dimensionless and normalized by t_c for the ambient porosity (Equation 28). The shear viscosity has an exponential dependence on porosity (Figure 5a).

4.7. Mechanisms of Porosity Generation

In the presented simulations, the modeled dehydration reaction, the porous fluid flow, and the solid deformation can affect the generation and evolution of ϕ . However, which mechanisms exactly produce ϕ and their relative importance is unclear. One reason is that in our coupled HMC model, most quantities, such as densities, fluid pressure, or fluid velocities, vary in space and time. We, therefore, first investigate the evolution of several quantities for S1. Due to the point symmetry of the vein formation with respect to the coordinate origin, we only show the upper, left half of the vein (Figure 13). The divergence of the solid velocity, $\nabla \cdot \mathbf{v}^s = \partial v_x^s / \partial x + \partial v_y^s / \partial y$, indicates a volumetric change associated with dehydration vein formation (Figure 13). A positive value of $\nabla \cdot \mathbf{v}^s$ indicates volume increase, or dilation (bordeaux colors in Figure 13). The solid velocities indicate mainly the applied far-field simple shear (black arrows in Figure 13), with some deviations around the dehydrating region. The fluid velocities (blue arrows in Figure 13) are completely different compared to the solid velocities. For the first time step, fluid flow only occurs in the central region where the porosity, and hence permeability, is high (Figure 13a). During dehydration vein formation, fluid flow mainly is localized along the boundaries of the veins which are characterized by higher values of $\nabla \cdot \mathbf{v}^s$ (Figures 13b–13d). The fluid velocities indicate fluid flow from the boundary of the dehydrating region toward the center of the vein (Figures 13b–13d). For the first time step,

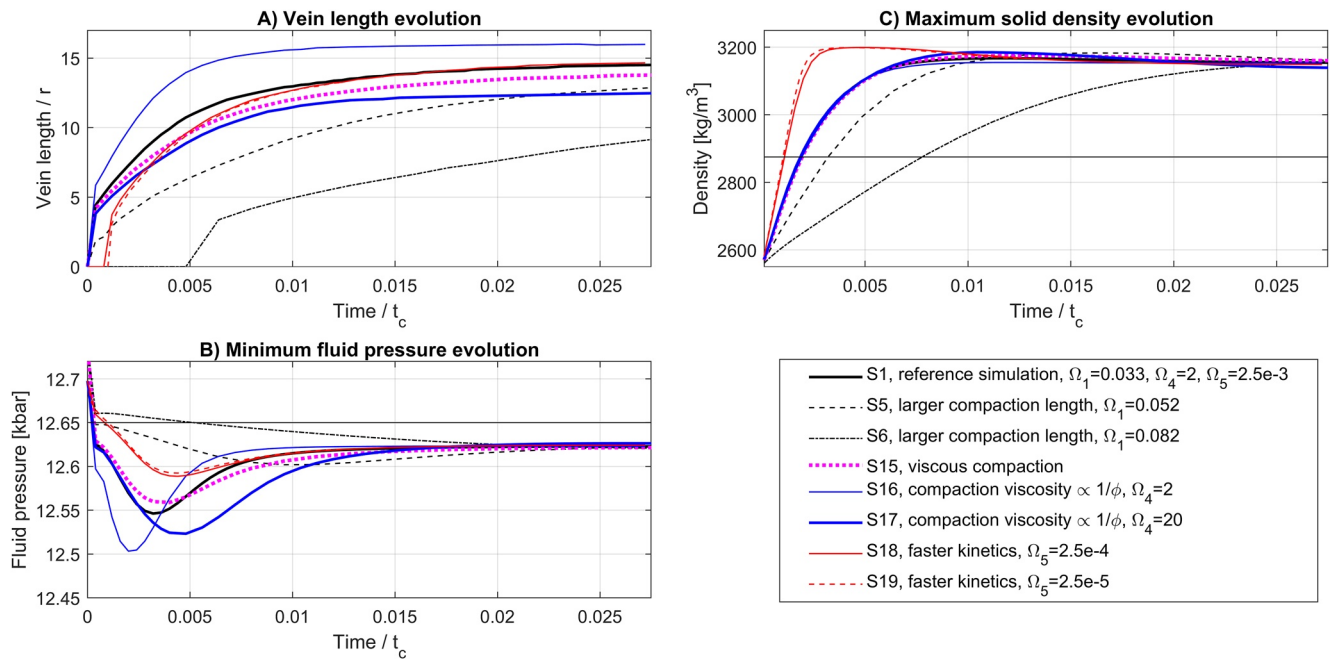


Figure 12. Time evolution of (a) dimensionless vein length, normalized by r , (b) minimum fluid pressure, and (c) maximum solid density, for the eight simulations indicated in the legend. Applied model parameters for the simulations are given in Table 2. Time displayed in panels is dimensionless and normalized by t_c for the ambient porosity (Equation 28).

the ϕ distribution indicates the initial, oblique Gaussian geometry (blue contour in Figure 13). With progressive deformation and vein formation, the region with higher ϕ grows in direction parallel to the dehydration vein. At the beginning of shearing, there is a small region with $p_f < 12.7$ kbar (red contours in Figure 13a) and this region is growing in a direction parallel to the vein. The region with $\rho_s > 2,700$ kg/m³ (dashed gray contours in Figures 13b–13d) also increases in direction parallel to the vein. In the early stages of shearing, nowhere in the model $\rho_s > 2,700$ kg/m³ since there are no contours for $\rho_s = 2,700$ kg/m³ (Figure 13a).

To quantify the relative contribution of the mechanisms controlling the temporal variation of ϕ , we post-process our numerical results (i.e., calculate values from saved numerical results). We quantify the mass transfer rate, Γ , associated with the dehydration reaction, which can be expressed by (using Equation 7):

$$\Gamma = -\frac{d(\rho_s(1-\phi))}{dt} - \rho_s(1-\phi)\nabla \cdot \mathbf{v}^s. \quad (30)$$

Note that in Equation 30 the material time derivative (d/dt , including the advection term, $\mathbf{v}^s \nabla \cdot [\rho_s(1-\phi)]$) is used and, hence, the divergence term is different compared to Equation 7. Therefore, Equation 30 represents an approximation of Γ since the advective term is not taken into account, here for simplicity of the post-processing. Equation 30 can be modified to yield:

$$\Gamma = \rho_s \frac{d\phi}{dt} - \rho_s(1-\phi)\nabla \cdot \mathbf{v}^s - (1-\phi) \frac{d\rho_s}{dt} \quad (31)$$

Importantly, in our HMC model Γ depends on the time derivative of ρ_s . This is not the case for HMC models assuming constant densities (e.g., Katz, 2008; their Equation 22). Equation 31 can be further rearranged to provide an expression for the temporal variation of the porosity:

$$\frac{1}{(1-\phi)} \frac{d\phi}{dt} = \nabla \cdot \mathbf{v}^s + \frac{1}{\rho_s} \frac{d\rho_s}{dt} + \frac{\Gamma}{\rho_s(1-\phi)} \quad (32)$$

Equation 32 shows that the temporal variation of the porosity is controlled by three mechanisms: (a) volumetric deformation of the solid (i.e., divergence of solid velocity field; first term on right-hand side of Equation 32), (b) temporal variation of solid density (second term) and (c) mass transfer of H₂O from the solid

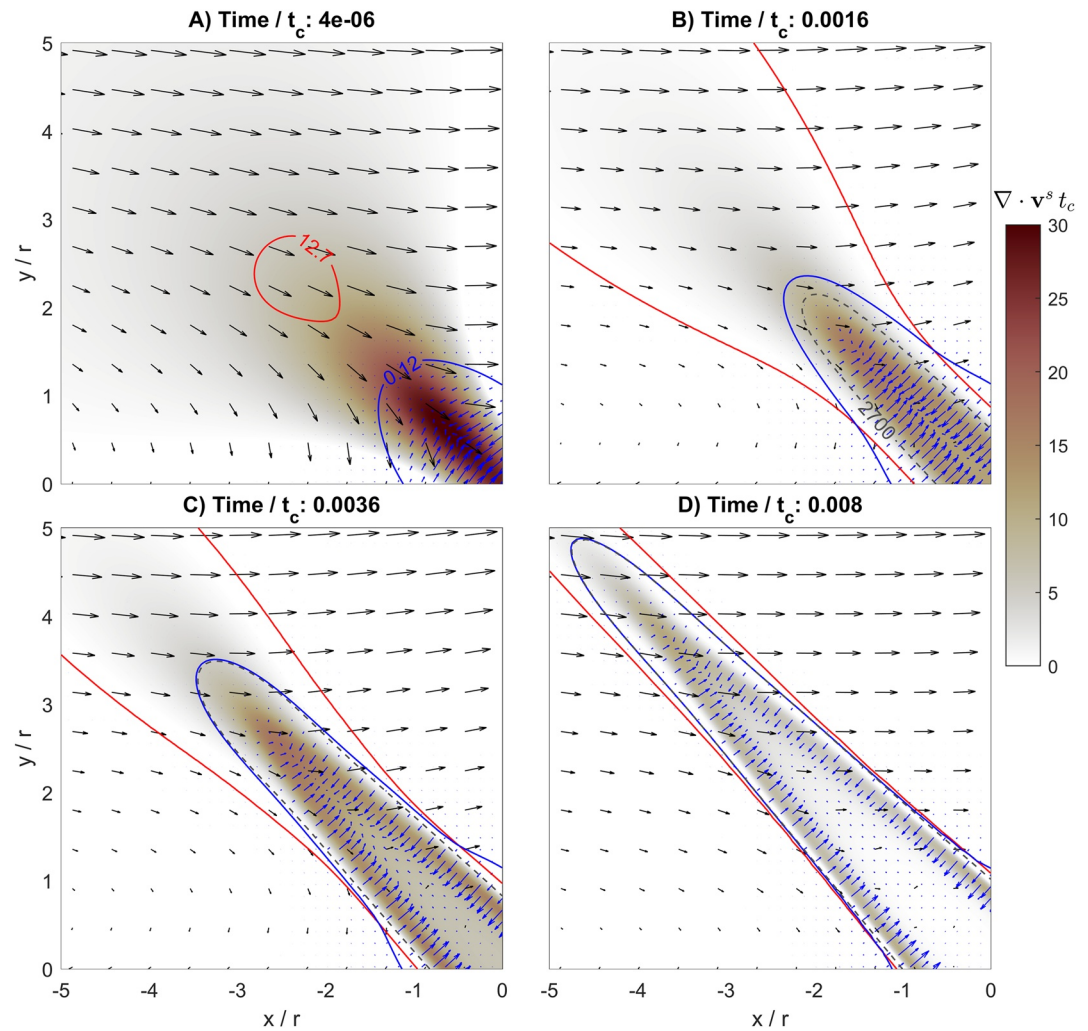


Figure 13. Evolution of the dehydration vein for the reference simulation S1. Applied model parameters are given in Table 2. Time displayed in panels is dimensionless and normalized by t_c for the ambient porosity (Equation 28). The colormaps show the dimensionless divergence of the solid velocity, the blue arrows show the fluid velocity field, and the black arrows show the solid velocity field. The red contour indicates fluid pressure, $p_f = 12.7$ kbar, whereby values of p_f are always smaller inside the contour. The blue contour indicates porosity, $\phi = 0.12$, whereby values of ϕ are always larger inside the contour. The dashed gray contour indicates solid density $\rho_s = 2,700$ kg/m³, whereby values of ρ_s are always larger inside the contour. There are no solid density contours in panel (a) because all densities are $< 2,700$ kg/m³.

to the fluid phase associated with the dehydration reaction (third term). We display the spatial distribution of the four terms in Equation 32 for S1 at a dimensionless time of 0.0036 (Figure 14). All four terms represent rates, have units of 1/s, such as the unit of solid volumetric deformation rate $\nabla \cdot \mathbf{v}^s$, and are normalized by multiplying with t_c for ϕ_a . The rate of ϕ , quantified by the term on the left-hand side of Equation 32, is positive and largest in the region of increased ϕ , indicating an increase of ϕ with time (Figure 14a). The sum of the three terms on the right-hand side of Equation 32 provides essentially the same result as the term on the left-hand side of Equation 32, indicating the accuracy of Equation 32 (Figures 14a and 14b). The magnitudes of the relative contributions of solid volumetric deformation (Figure 14c), solid density variation (Figure 14d) and mass transfer (Figure 14e) to the temporal variation of porosity are different, because the magnitudes of these three terms are different (Figures 14c–14e).

To investigate the temporal variation of the relative importance of solid volumetric deformation rate, solid density rate and mass transfer rate on the rate of ϕ , we record the maximum value of each rate for each numerical time step and plot these maximum rates versus the dimensionless model time (Figure 15). Solid density and mass

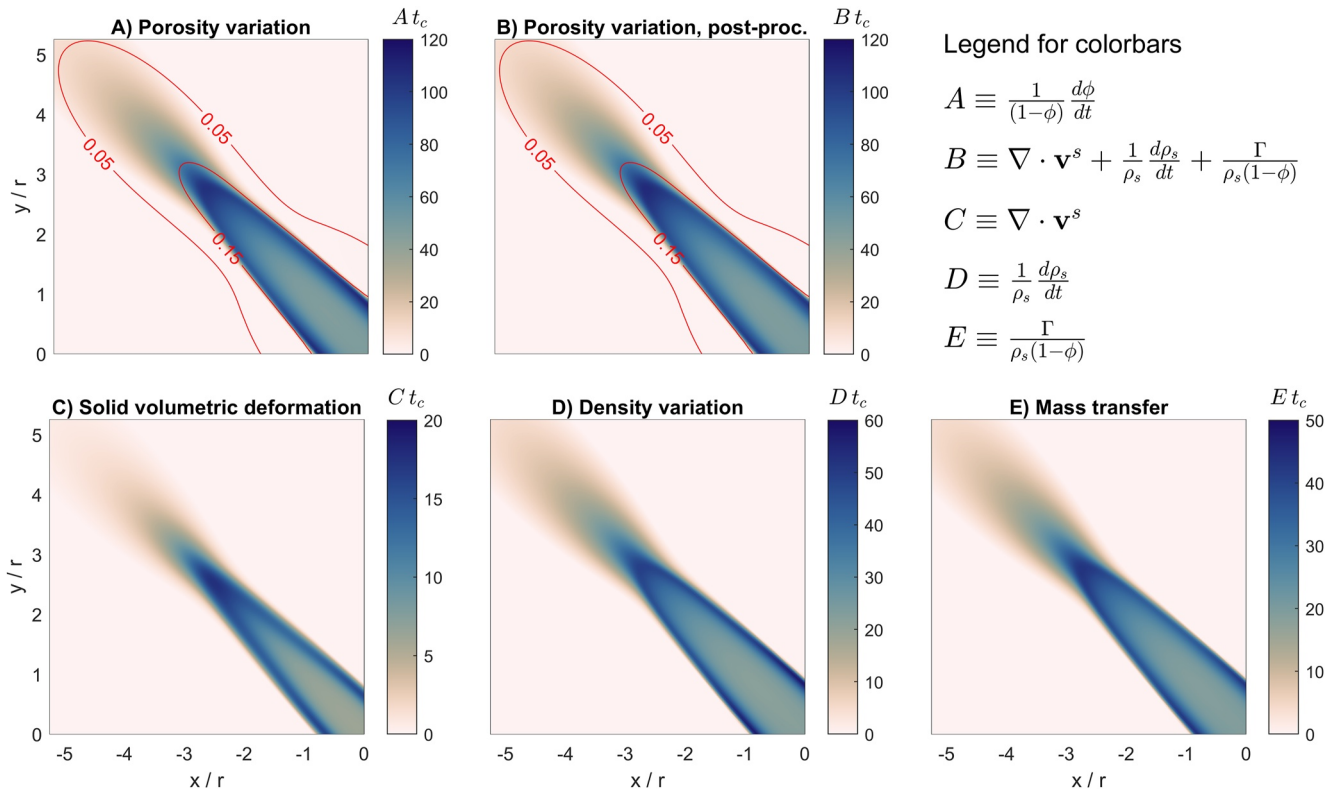


Figure 14. The three mechanisms that control the temporal porosity variation (see Equation 32) for the reference simulation S1 at a dimensionless time of 0.0036. Panel (a) shows the colormap of the quantity displayed in the legend for (a), which represents the porosity rate, panel (b) shows the colormap of the quantity displayed in the legend for (b), panel (c) shows the colormap of the quantity displayed in the legend for (c), which represents the rate of solid volumetric deformation, panel (d) shows the colormap of the quantity displayed in the legend for (d), which represents the rate of solid density variation, and panel (e) shows the colormap of the quantity displayed in the legend for (e), which represents the rate of mass transfer. All displayed terms represent dimensionless rates which are normalized by t_c for the ambient porosity (Equation 28). Symbols are explained in Table 1 and applied model parameters are given in Table 2.

transfer rates overall decrease during the model evolution (Figure 15). The rate of solid volume change first increases and then decreases again (Figure 15). In summary, the results for S1 indicate that the rate of solid density change has the strongest and the rate of solid volume change the smallest contribution to ϕ generation. However, the rate of solid volume change has a nonnegligible contribution to ϕ generation.

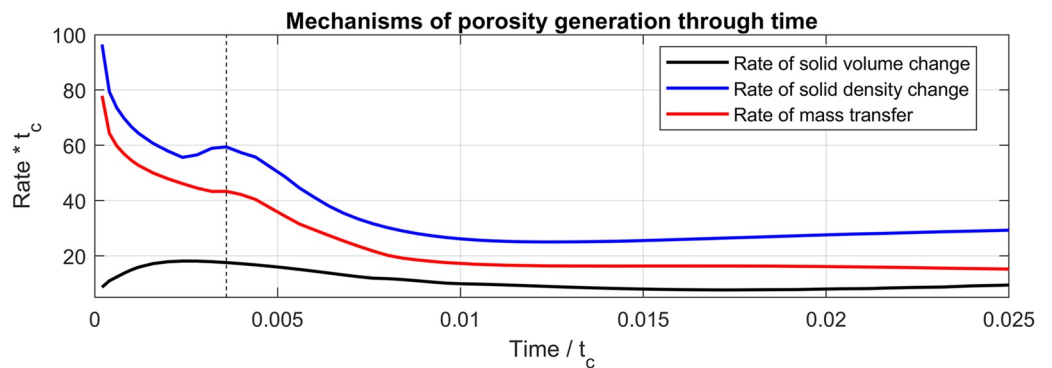


Figure 15. Time evolution of the maximum (per each time step) values of the rate of solid volume change (quantity labeled C in Figure 14), rate of solid density change (quantity labeled D in Figure 14) and rate of mass transfer (quantity labeled E in Figure 14). Results correspond to the reference simulation S1 (see Table 2). Time is dimensionless and normalized by t_c for the ambient porosity (Equation 28). The vertical dashed line indicates the time for which results are displayed in Figure 14.

5. Discussion

5.1. Shear-Driven Dehydration and Olivine Vein Formation

Field observations have led previous authors to hypothesize that en échelon metamorphic olivine veins are caused by shear deformation, but this hypothesis has not been tested with a HMC model. Our simulations show that it is hydrologically, mechanically, and chemically possible to form olivine veins by dehydration reactions which are triggered during ductile shearing of serpentinite. A thermodynamic reaction, such as the dehydration reaction considered here, is typically controlled by a narrow zone in pressure-temperature space (e.g., Figures 2e and 3). In isothermal models, such as the one presented here, the reaction occurs, therefore, across a narrow pressure range (Figure 3c). In our model, we assume that the fluid pressure, p_f , controls the reaction which is supported by theoretical and experimental studies (e.g., Dahlen, 1992; Llana-Fúnez et al., 2012). The p_f is initially homogeneous and everywhere in the model domain within the serpentinite stability field, and represents the ambient fluid pressure, p_a . Only if p_a is close to the reaction pressure and if the shear-driven p_f perturbations are significant, then p_f can decrease locally below the reaction pressure during shearing and trigger the dehydration reaction (Figure 7). For our model configuration, p_a of 13.5 kbar is close enough to trigger dehydration for a reaction pressure of 12.65 kbar (pressure difference of 0.85 kbar; Figure 7). Assuming an average density of the overlying rock of 3,000 kg/m³ for this pressure difference, the dehydration can be triggered when the rocks are within a vertical distance of approximately 2.5–3 km to the depth at which the reaction would occur with respect to a lithostatic pressure.

Our model for shear-driven dehydration is distinct from other published models of similar dehydration reactions (e.g., Huber et al., 2022; Malvoisin et al., 2015; Schmalholz et al., 2020). This is because those models employ an initially heterogeneous distribution of p_f , where the initial values of p_f already correspond to the stability fields on both sides of the reaction (e.g., Huber et al., 2022; Malvoisin et al., 2015; Schmalholz et al., 2020). Therefore, the initial condition in these models guarantees that the initial p_f will trigger the dehydration reaction. In contrast, in our model the evolution of a heterogeneous p_f distribution is simulated (Figure 6). Whether this evolving p_f distribution can trigger dehydration and eventually generate an olivine vein, depends on the applied value of p_a and model parameters, such as the applied relation between δ/r and ϕ (Figures 7–9). Only if the fluid pressure decreases locally below the reaction pressure, an olivine vein can form. Consequently, our model predicts that mechanical deformation is a potential mechanism for the formation of dehydration veins. An alternative possibility for triggering local dehydration, is an initially heterogeneous chemical composition of the serpentinite. For example, some regions in the serpentinite having brucite would dehydrate while other regions exclusively composed of antigorite would not dehydrate (e.g., Plümper et al., 2017). Such chemical mechanism does not require any solid deformation. However, for such a mechanism the orientation of the olivine veins is entirely controlled by the initial chemical composition. The specific en échelon geometry of olivine veins is most likely not caused by initial chemical heterogeneity in a non-deforming rock, especially since these veins are formed in a strongly sheared antigorite serpentinite.

Field data show that in the Erro Tobbio region the olivine in the studied veins is indeed metamorphic olivine, which is also supported by geochemical studies (e.g., Peters et al., 2020). Furthermore, in all presented simulations, the formation of dehydration veins is not a run-away process, but a self-limiting process (Figures 6 and 12). Hence, the simulation with initial random porosity perturbation shows the formation of several veins with similar length, which stop growing after some amount of shear (Figure 11). The simulation does not show the formation of a single vein which grows across the entire model domain (Figure 11). The formation of many veins of similar size and orientation, and the absence of few, large veins agree with natural observations (Figure 1). Therefore, based on published geochemical studies, structural observations, and our modeling results, we propose that the formation of observed olivine veins was the result of a coupled deformation-reaction process that accelerated mineral dehydration along orientations, controlled by the local stress field in the sheared serpentinite. Similar veins made of metamorphic olivine have been described from subducted serpentinite, such as in the Zermatt-Saas unit in the Central Alps (e.g., Kempf et al., 2020).

5.2. Scaling to Dimensional Parameters

We assume now particular values for the model parameters and discuss the applicability and consequences of the applied dimensionless numbers, Equation 29 and Table 2, for the natural situation. We assume $\eta_s = 10^{17}$ Pa·s.

Despite the importance of serpentinite, its rheology at lithospheric-scale pressure and temperature conditions remains not well constrained (e.g., E. C. David et al., 2018; Hirauchi et al., 2020, and references therein). However, for the ambient pressure and temperature conditions considered here, viscosities of serpentinite of approximately 10^{17} Pa·s seem feasible based on experimental studies (e.g., Chernak & Hirth, 2010; Hilairet et al., 2007). We further assume $\eta_f = 10^{-3}$ Pa·s, $\phi_a = 0.02$ and $r = 10$ cm. Applied values of Ω_1 range between 0.012 and 0.33 and we mainly applied $\Omega_4 = \zeta/\eta_s = 2$ (Table 2). For the values assumed above, values of Ω_1 between 0.012 and 0.33 require values for the product $k\phi_a^3$, which represents the ambient permeability, approximately between 4×10^{-27} and 3×10^{-24} m², respectively. Note, that we could have also used the permeability formulation $k\phi^3 = k\phi_a^3(\phi/\phi_a)^3 = k_0(\phi/\phi_a)^3$ and then k_0 would represent the ambient permeability. Such values for $k\phi_a^3$ indicate that the serpentinite should be essentially impermeable in the regions where the olivine veins form. Experimental studies suggest that serpentinite permeability decreases exponentially with depth and is in the order of 10^{-23} and 10^{-21} m² at a depth of 7 km below seafloor (e.g., Hatakeyama et al., 2017). Permeabilities at much greater depth and ambient pressure, as the 12.75 kbar ambient pressure considered here, could hence be smaller than 10^{-23} m². The extrapolation of Hatakeyama et al. (2017) (their Equation 1), for their serpentinite termed Sengen-03, suggests a permeability of 10^{-26} m² already for a confining pressure of approximately 6 kbar. Therefore, permeabilities between 10^{-24} and 10^{-26} m², or in other words an effectively impermeable serpentinite as required in our models, is not unrealistic for natural serpentinite under a confining pressure of approximately 12.75 kbar and the assumed temperature of 500°C. Furthermore, η_s could have potentially been smaller than 10^{17} Pa·s during significant shearing, for example, due to a strongly nonlinear deformation behavior as mimicked here with a pressure-insensitive yield stress, so that required values for $k\phi_a^3$ could also have been larger than 10^{-24} m², keeping values of Ω_1 the same.

For Ω_2 we applied a value of 0.11 which requires a value of \bar{D}_{xy} of approximately 10^{-9} s⁻¹. For a typical subduction velocity of 3 cm/yr, a shear zone must be 1 m thick so that a relative shear velocity across the shear zone generates a shearing rate of 10^{-9} s⁻¹. Such strain rate and $\eta_s = 10^{17}$ Pa·s generates a shear stress in the order of 100 MPa. We also applied a yield stress in some simulations to limit shear stresses to 100 MPa (Figures 10a–10d and 11). Such shear stresses agree with recent studies that estimate shear stresses between 40 and 160 MPa at subduction interfaces (e.g., England, 2018; England & Smye, 2023). Fast shearing rates of 10^{-9} s⁻¹ are presumably more likely achieved during aseismic slow slip events, whereby shearing velocities are larger than a few centimeters per year. For example, typical slip velocities associated with long term slow slip events are between 35 and 70 cm/yr (1–2 mm/day; see review of Behr & Bürgmann (2021), and references therein) and for such faster slip velocities strain rates of 10^{-9} s⁻¹ are achievable in shear zones with thicknesses of up to approximately 20 m.

For the parameters assumed above, for $k\phi_a^3 = 10^{-25}$ m² and for a typical solid bulk modulus $K_s = 10^{11}$ Pa, the characteristic time (t_c , Equation 28) for ϕ_a is approximately 30 years. The typical dimensionless time at which simulations reached a steady-state, where minimum values of p_f and maximum values of ρ_s stopped changing considerably, is approximately 0.025 (Figure 12). This dimensionless time corresponds then to a natural duration of approximately 10 months. For $k\phi_a^3 = 10^{-24}$ m², the duration is approximately 1 month. The applied value of $\Omega_5 = t_{kin}/t_c = 0.0025$ means that the characteristic kinetic time should be at least one order of magnitude shorter than the typical time, or duration, of the vein formation. This means that the kinetic time should be shorter than 1 or 0.1 months (3 days) for values of $k\phi_a^3$ of 10^{-25} m² or 10^{-24} m², respectively. For values of $\zeta = 2 \cdot 10^{17}$ Pa·s and $K_d = K_s/2 = 5 \cdot 10^{10}$ Pa, the visco-elastic Maxwell time, $t_{Max} = \zeta/K_d$, is approximately 1.5 months. The value of $\Omega_6 = t_{Max}/t_c$ is then 0.004 if t_c is calculated with $k\phi_a^3 = 10^{-25}$ m². This value is close to the applied value of $\Omega_6 = 0.001$ (Table 2).

In summary, the scaling shows that the applied dimensionless parameters are applicable to a natural situation of shear-driven olivine vein formation, where serpentinite is effectively impermeable and shear deformation is fast, potentially resulting from aseismic slow slip events.

In future studies, we aim to potentially elaborate the applied dimensionless parameters and characteristic scales. For example, the reaction and porous flow is controlled in our model by the amplitude of the fluid pressure perturbation. A systematic analysis might reveal the parameters that control both the maximum amplitude and the quasi-steady-state amplitude of the fluid pressure perturbation (Figure 12b). Also, we aim to eventually determine another characteristic time scale that enables to collapse the different curves of maximum solid density versus time onto a single characteristic curve (Figure 12c).

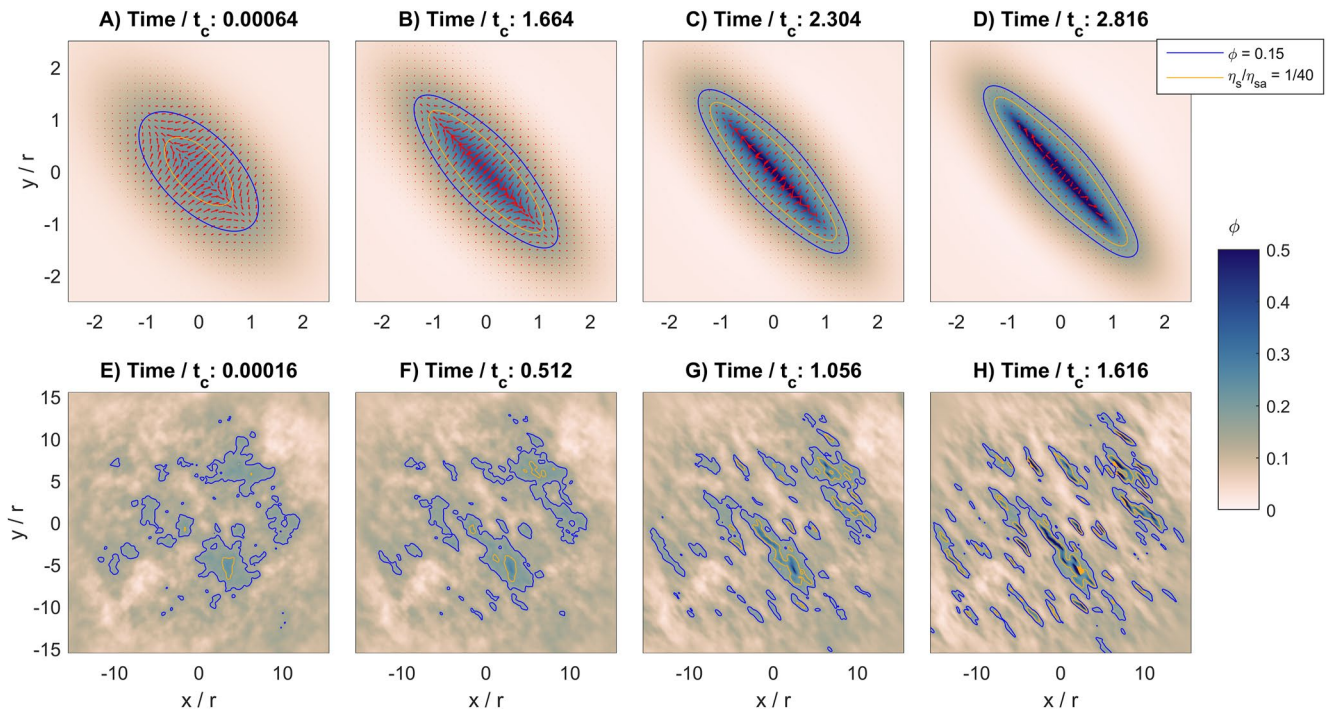


Figure 16. Formation of localized, high-porosity fluid bands without dehydration reaction for simulations S20 and S21 (see Table 2). Color plots show porosity, ϕ . Time is dimensionless and normalized by t_c , blue contours indicate $\phi = 0.15$ and orange contours indicate viscosities of $\eta_s/\eta_{sa} = 1/40$. Panels (a–d) show color plots of ϕ for the simulation S20. Red arrows indicate fluid velocity. Panels (e–h) show the simulation S21. The total area within the orange contour lines is increasing with time, indicating an effective weakening of the model domain due to the increase in areas with $\eta_s/\eta_{sa} < 1/40$. Regions with high ϕ become elongated and parallel to the orientation of σ_1 (see Figure 4).

5.3. Shear-Driven High-Porosity Fluid Bands Without Dehydration

In S2 with $p_a = 14.5$ kbar, in which no dehydration reaction occurs (Figures 7a–7d), one might expect the formation of elongated regions with increased ϕ due to a process similar to the process that forms localized melt bands during simple shearing of partially molten rock (e.g., Holtzman et al., 2003; Katz et al., 2006; Spiegelman, 2003; Stevenson, 1989). However, in the simulation with $p_a = 14.5$ kbar no such bands with high ϕ formed (Figures 7a–7d). One reason might be that the characteristic time scale of fluid flow, t_c , is too short with respect to the duration of shearing, because the final dimensionless time of the simulation with $p_a = 14.5$ kbar is 0.176 (Figure 7d). This means that t_c is approximately a factor of 5 longer than the duration of the simulation. To test the impact of t_c , we performed simulation S20 with $p_a = 14.5$ kbar and with a value of $k\phi_a^3$ that is 100 times larger compared to S1. Therefore, t_c in S20 is 100 times shorter compared to S1 and the corresponding Ω_1 is 10 times larger, namely $\Omega_1 = 0.33$ (Figures 16a–16d). For such values of t_c and Ω_1 , the simulation shows indeed the formation of an elongated region with high ϕ which is oriented parallel to the orientation of σ_1 (Figures 16a–16d). We also performed simulation S21 with an initially random perturbation, with $p_a = 14.5$ kbar, and for the same values of t_c and $\Omega_1 = 0.33$ as for S20. S21 also shows the formation of elongated regions of high ϕ , oriented parallel to σ_1 (Figures 16e–16h). For S20 and S21, the final dimensionless time is >1 , indicating that t_c is shorter than the duration of shearing so that significant fluid flow can occur during the shearing. S20 and S21 show that during shearing of serpentinite without reaction, that is during the formation of serpentinite mylonites, elongated high-porosity regions, with lower shear viscosity can form. The formation of such elongated high-porosity regions could have been one mechanism causing the formation of shear bands in the antigorite serpentinite which are frequently observed in the Erro Tobbio region (e.g., Hermann et al., 2000; Scambelluri et al., 1995). Once p_a will become close to the reaction pressure, due to continued burial, these high-porosity, low-viscosity fluid bands might then have favored the generation of olivine veins, similar to our simulations with an oblique initial Gaussian ϕ distribution.

5.4. Simplifications

The modeled process involves the coupling of a metamorphic reaction, significant density changes, porous fluid flow and rock deformation. Therefore, the studied process and the applied HMC model are already quite complex. On the other hand, we simplified each of the hydraulic, mechanical, and chemical processes to develop a mathematical model that is still transparent and relatively easy to solve numerically.

For the hydraulic process, we consider a standard Darcy flow model with an isotropic permeability that has a cubic dependence on ϕ ($k\phi^3$). The exponent of ϕ can also differ from 3 and values between 1 and 25 have been reported (e.g., C. David et al., 1994). Furthermore, this exponent can also vary during a compaction process (e.g., Hommel et al., 2018), the porosity-permeability relations could be more complex (e.g., Costa, 2006; Hommel et al., 2018) and/or the porosity-permeability relation could also be spatially variable in the serpentinite. Therefore, there is considerable uncertainty concerning the natural porosity-permeability relation in the serpentinite, especially at 12.75 kbar and 500°C ambient pressure and temperature, respectively.

For the mechanical shearing process, we consider a flow law in which the shear viscosity is only a function of porosity. In a natural serpentinite with constant porosity, the relationship between deviatoric stress and strain rate could be nonlinear due to an effective shear viscosity that depends on the stress magnitude, the mineral grain size, and the chemical composition. Such nonlinearity can be mathematically represented by a power-law relationship between deviatoric stress, τ , and strain rate, D , of the form $\tau^m \approx D$ (e.g., Montesi & Zuber, 2002). If $m \gg 1$, then τ increases insignificantly with increasing D . To test the impact of such nonlinear stress-strain rate relationships, we have also performed simulations with a pressure-insensitive yield stress, in which stress remains constant for increasing strain rate and which represents a considerably nonlinear flow law for $m \gg 1$. Concerning the effective shear viscosities: During olivine vein formation, ρ_s changes continuously from ρ_s for serpentinite to ρ_s for olivine indicating a transient transformation from antigorite + brucite to forsterite (Figure 12c). Furthermore, in modeled regions with $\rho_s > 3,000 \text{ kg/m}^3$, values of $\phi > 0.4$ (Figure 11). In nature, the fluid is likely distributed along mineral grain boundaries and we assume that a mixture of grains, transforming from antigorite + brucite to forsterite, and fluid with $\phi > 0.4$ has a low effective shear viscosity. An individual, fully transformed forsterite grain has a much larger shear viscosity and could potentially also deform in a frictional-plastic manner at 500°C. Moreover, we apply a constant value of a for the exponential relationship between η_s and ϕ (Equation 16) over the entire ϕ range between 0.02 and ~ 0.5 . However, a could also vary with ϕ , especially for higher values of $\phi > 0.2$.

For the chemical process, we consider for simplicity a fixed chemical composition for which forsterite + water results from dehydration of antigorite + brucite + a small amount of free water. We consider this small amount of free water simply to be able to apply the governing two-phase equations for solid-fluid mixtures in the entire model domain and to calculate thermodynamically the fluid density in the stability field of antigorite + brucite (Figure 3c). Natural chemical compositions, in for example, the Erro-Tobbio unit, are more complex and feature a higher chemical variability as considered in our model. However, the main aim of our study is to investigate the fundamental coupling between dehydration reactions, density changes, fluid flow and rock deformation, justifying the use of a simplified MSH system. A more elaborated system would be the FMASH system which also considers aluminum, Al, and iron, Fe (e.g., Padrón-Navarta et al., 2013). One effect of the FMASH system, applied to our isothermal model, would be that both brucite and olivine could be stable at the same pressure over a range of pressure, within a so-called divariant field (e.g., Padrón-Navarta et al., 2013). Consequently, the H₂O liberation would not be controlled by a specific pressure but would rather occur over a pressure interval. Such a pressure interval is already considered in our model because the modeled reaction does not occur sharply at one specific fluid pressure, but over an interval between 12.6 and 12.7 kbar. Considering a FMASH system would allow to constrain this pressure interval better. Furthermore, our model suggests that natural areas of serpentinite dehydration, consisting of olivine and water, are mechanically weak due to their high, up to 0.5, porosity, and water content as proposed by Hermann et al. (2000). After the formation of the dehydration veins, the water eventually escapes the dehydration region, so that finally only olivine is left in the veins.

5.5. Potential Applications to Deep-Seated Slow Slip and Tremor

The presented model could potentially be applied to investigate fluid-related processes causing episodic tremor and slow slip events (ETS; e.g., Behr & Bürgmann, 2021; Peng & Gombert, 2010). Despite the lack of consensus on the inter-relationships between dehydration, fluid flow, critical stress and ETS, the coincidence of the

location of low-frequency earthquakes to regions with high V_p/V_s ratios requires the consideration of fluid flow and dehydration in these settings (e.g., Behr & Bürgmann, 2021; Burlini et al., 2009; Kato et al., 2010; Shelly et al., 2007; Van Avendonk et al., 2010). For example, Van Avendonk et al. (2010) infer a zone of very high V_p/V_s of 6 at the top of the subducting Cocos slab between 35 and 55 km depth, lying down-dip of the seismogenic zone. They propose that these high V_p/V_s ratios are due to several-meter thick shear zones under high pore pressure and that the hydrous pore fluids were generated by prograde dehydration reactions. The 35–55 km depth range with inferred high V_p/V_s ratios corresponds to the depth range and ambient pressure considered in our model. In addition, the correlation of rapid-tremor migration to pore-pressure waves suggests that this coincidence can be explained by the coupled processes of dehydration, fault weakening and tremor migration (Cruz-Atienza et al., 2018). Thus, the formation of fluid-filled veins, as modeled here, can be correlated to the transient weakening that is inferred in regions of dehydration. Furthermore, the dehydration reaction, generating olivine-fluid bearing veins, and the subsequent fluid escape, leaving behind olivine-only veins, will cause a viscosity inversion: when significant fluid is present in the olivine bearing veins, then the effective viscosity of the olivine-fluid veins is smaller than the viscosity of the serpentinite; but once the fluid has escaped the veins the effective viscosity of the olivine-only veins is larger than the viscosity of the serpentinite. Such viscosity variation and inversion likely strongly impact the spatial and temporal distribution of stresses. We predict that, under the presence of a general anisotropic stress field, the vein formation will lead to an increase of the anisotropic effective viscosity of the subducted mantle rocks because of the different effective viscosities of serpentinite and olivine + fluid assemblages. When the fluid is completely drained from these veins, the anisotropy and viscosity contrast between olivine and serpentinite will be permanent.

6. Conclusions

We developed a 2D hydro-mechanical-chemical model to study the formation of olivine veins caused by the dehydration of serpentinite during ductile deformation. The model considers the reaction antigorite + brucite = forsterite + water and the significant changes in solid density resulting from this reaction. The model predicts shear-driven formation of olivine dehydration veins and, hence, supports the hypothesis of shear-driven formation of metamorphic olivine veins in the antigorite serpentinites of the Erro Tobbio unit (Figure 1).

The fluid and total pressures are initially homogeneous in the model and correspond to the serpentinite stability field. The applied model, hence, does not a priori prescribe that dehydration takes place. In contrast, the model can predict the self-consistent generation of fluid pressure perturbations during shearing of mechanically heterogeneous serpentinite, which spontaneously trigger the dehydration reaction and cause the formation of olivine veins. The modeled veins consist of a weak forsterite-water mixture and grow in a direction parallel to the maximum principal stress which is controlled by the applied far-field simple shear. The modeled growth of dehydration veins is not an unstable, or runaway, process, but a self-limiting process because minimum values of fluid pressure and the vein length eventually reach a steady state.

The applied initial porosity geometry, a pressure-insensitive yield strength, mimicking a strongly stress dependent effective viscosity, an elastic component of compaction, the dependence of the compaction viscosity on the inverse of porosity and reaction kinetics have a minor impact on olivine vein formation in our simulations. Conversely, the applied ambient fluid pressure and the relationship between compaction length and porosity have a strong impact. For the applied model configuration, a shear viscosity with exponential dependence on porosity provides a compaction length which first increases and subsequently decreases with increasing porosity and is suitable for the formation of olivine veins.

The rate of porosity generation during dehydration is controlled by the rates of three mechanisms: the rate of solid volumetric change, the rate of solid density change and the rate of reactive mass transfer. All three mechanisms contribute to the porosity generation during shearing. In the performed simulations, the rate of solid density change had the strongest and the rate of solid volumetric change the weakest impact on porosity generation.

Olivine veins are observed in several high-pressure serpentinites in the Western Alps and Liguria. The modeled veins have a similar orientation as natural en échelon olivine veins in serpentinite mylonite. The self-limiting feature of the modeled vein growth might also explain the natural observation of many smaller olivine veins and the absence of few large olivine veins. Furthermore, the presented model can explain transient weakening and the generation of mechanical anisotropy during dehydration when the elongated, parallel, and high-porosity

veins consist of a fluid-olivine mixture. The eventual escape of the fluids will cause a viscosity and anisotropy inversion since olivine-only veins are stronger than serpentinite. Such transient weakening, anisotropy generation and viscosity inversion may be important processes during slow slip and tremor observed at subduction zones. Rescaling of the model results to natural conditions suggests that the natural serpentinite should have been effectively impermeable, with ambient permeabilities smaller than approximately 10^{-24} m², during olivine vein formation and the shearing rate should have been in the order of 10^{-9} s⁻¹, presumably during periods of slow slip.

Appendix A

A1. Numerical Algorithm

To determine the unknowns p_f , p , ϕ , v_x^s and v_y^s we employ the iterative accelerated PT method (Räss et al., 2022) using a finite difference discretization on a regular Cartesian staggered grid, described in Schmalholz et al. (2020). For example, Equation 10 is used to solve for ϕ . Therefore, a PT derivative of ϕ , written as $\Delta^{PT} \phi / \Delta t_\phi^{PT}$, is added to the left-hand side of Equation 10, which yields

$$\frac{\Delta^{PT} \phi}{\Delta t_\phi^{PT}} = \frac{\partial}{\partial t} [\rho_X (1 - \phi)] + \nabla \cdot [\rho_X (1 - \phi) \mathbf{v}^s]. \quad (\text{A1})$$

Within a PT iteration loop the value of ϕ is iteratively updated and the value of $\Delta^{PT} \phi / \Delta t_\phi^{PT}$ converges toward zero during the iterations. The iterations are stopped once the value of $\Delta^{PT} \phi / \Delta t_\phi^{PT}$ is smaller than a specified tolerance value. This tolerance value corresponds to the residual of the numerically solved PDE (see also Halter et al., 2022). The unknowns p_f , p , v_x^s and v_y^s are determined with the same PT method within the same iteration loop. The system of PT equations is:

$$\begin{aligned} \frac{\Delta^{PT} p_f}{\Delta t_{p_f}^{PT}} &= -\frac{\partial \rho_T}{\partial t} + \nabla \cdot \left[\rho_f \frac{k \phi^3}{\eta_f} \nabla p_f \right] - \nabla \cdot (\rho_T \mathbf{v}^s) \\ \frac{\Delta^{PT} \phi}{\Delta t_\phi^{PT}} &= \frac{\partial}{\partial t} [\rho_s X_s (1 - \phi)] + \nabla \cdot [\rho_s X_s (1 - \phi) \mathbf{v}^s] \\ \frac{\Delta^{PT} v_i^s}{\Delta t_v^{PT}} &= \nabla \cdot \sigma_{ij} \\ \frac{\Delta^{PT} p}{\Delta t_p^{PT}} &= -\nabla \cdot \mathbf{v}^s - \frac{1}{K_d} \left(\frac{dp}{dt} - \alpha \frac{dp_f}{dt} \right) - \frac{p - p_f}{(1 - \phi) \zeta} \end{aligned} \quad (\text{A2})$$

To discretize the physical time derivatives, such as $\partial \rho_T / \partial t$, we employ a “physical” time step, Δt . The applied values of Δt and of the PT, Δt^{PT} , time steps are typically:

$$\begin{aligned} \Delta t &= 4 \times 10^{-6} \frac{r^2 \eta_f}{k \phi_a^3 K_s} \\ \Delta t_\phi^{PT} &= \Delta t \\ \Delta t_{p_f}^{PT} &= C_{p_f} \frac{\max(\Delta x, \Delta y)^2}{\max\left(\frac{k \phi^3 K_s}{\eta_f}\right)} \\ \Delta t_v^{PT} &= C_v \frac{\max(\Delta x, \Delta y)^2}{\max(\eta^s)} \\ \Delta t_p^{PT} &= C_p \frac{\max(\eta^s) \Delta x}{w} \end{aligned} \quad (\text{A3})$$

where Δx and Δy are horizontal and vertical numerical grid spacing, respectively, and the values of the factors C_{p_f} , C_v , and C_p can vary for different simulations, mainly to reduce the number of required PT iteration loops. More information concerning the choice of such PT time steps can be found in Räss et al. (2022) and Wang et al. (2022). Upon convergence, these iterations provide results which are equivalent to results of a numerical-implicit method, since the gradients of the numerical variables are updated in each iteration.

For reasons of numerical efficiency, we approximate the thermodynamic relations of the densities and mass fractions with the fluid pressure, obtained with Gibbs free-energy minimization, with analytical functions (Figures 3c and 3d):

$$\begin{aligned} \rho_f &= 1194 \times \ln\left(\frac{p_f}{p_{ini}} + 1\right)^{1/3.5} \\ \rho_s^{EQ} &= -\tanh\left(600 \times \frac{p_f - p_R}{p_{ini}}\right) \times 323.32 + 2848 + \left(\frac{p_f}{p_{ini}} - 0.0078\right) \times 30.4762 \\ X_s^{EQ} &= -\tanh\left(600 \times \frac{p_f - p_R}{p_{ini}}\right) \times 0.1292 + 0.8707 \end{aligned} \quad (A4)$$

where p_R is the reaction pressure, here 12.65 kbar. We use the functions above in the numerical algorithm to calculate densities and mass fraction from the current fluid pressure. We provide a general overview, in the form of a simple flowchart, of the structure of the numerical algorithm and the order of the governing equations in which they are solved within the iteration loop in Figure A1.

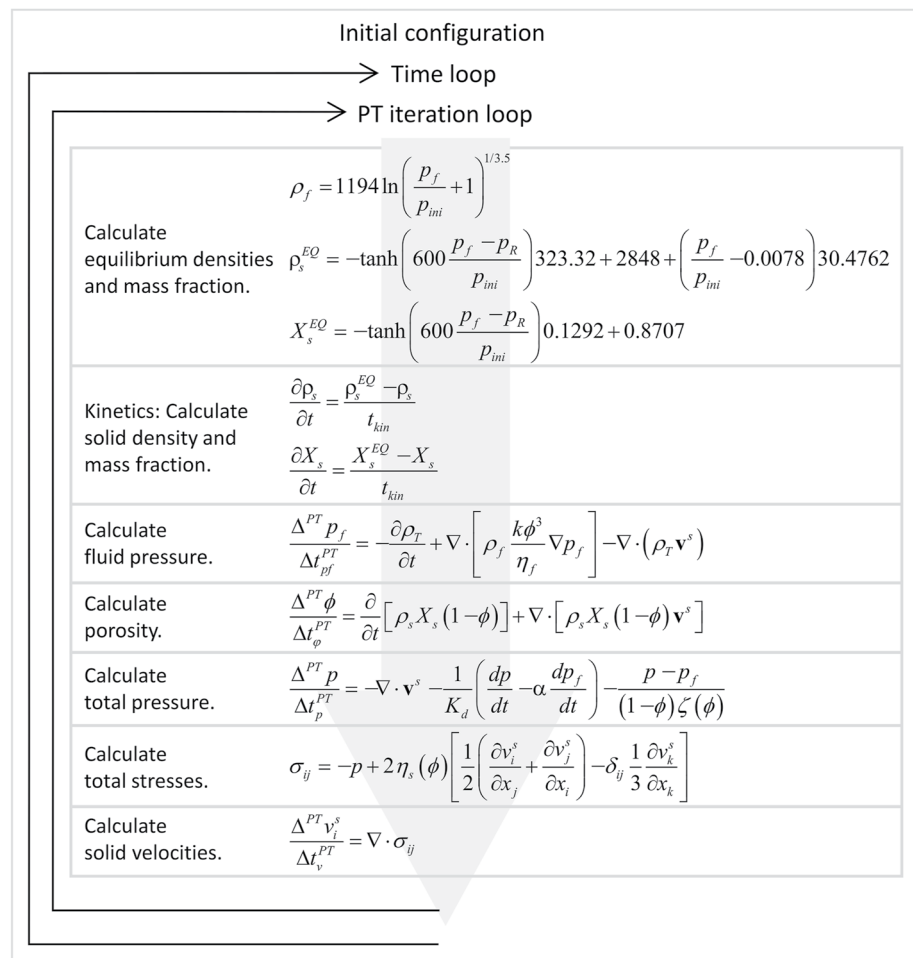


Figure A1. Simplified flow chart of the applied numerical algorithm and the order of the equations in which they are solved inside the pseudo-transient (PT) iteration loop. The PT iteration loop calculates the unknowns and simultaneously treats the various nonlinearities, such as porosity-dependent shear viscosity and permeability. The time loop calculates the evolution of the unknowns with time. Symbols are explained in Table 1.

A2. Numerical Resolution and Accuracy Test

We present here the results of a numerical resolution and accuracy test. Such tests are essential to determine whether the evolution of the dehydrating region is independent of (a) the employed numerical resolution and (b) the applied tolerance to exit the PT iteration loop. We performed the simulation S1 with the following different numerical resolutions: 300×300 , 500×500 , 700×700 , 900×900 and $1,100 \times 1,100$ grid points (Figure A2). For a dimensionless model time of 0.0152, the ratio of the maximum porosity in the model domain divided by the maximum porosity for a simulation with $1,100 \times 1,100$ grid points is plotted versus the corresponding resolution for simulations with different resolution (Figure A2a). Similar ratios are plotted for the minimum fluid pressure in the model domain and the average value of the fluid velocity. The higher the resolution, the less the three ratios vary, indicating the convergence of the numerical results upon increasing numerical resolution. The differences for the minimum fluid pressure are so small (see Figure A2b) that they are hardly visible. The evolution of the minimum fluid pressure in the model domain with time is shown for different numerical resolutions (Figure A2b). With larger numerical resolution, the temporal evolution of the minimum fluid pressure varies less, indicating again the convergence of the numerical results for increasing numerical resolution. Finally, the spatial distribution of p_f at a dimensionless time of 0.0152 is displayed for three different resolutions

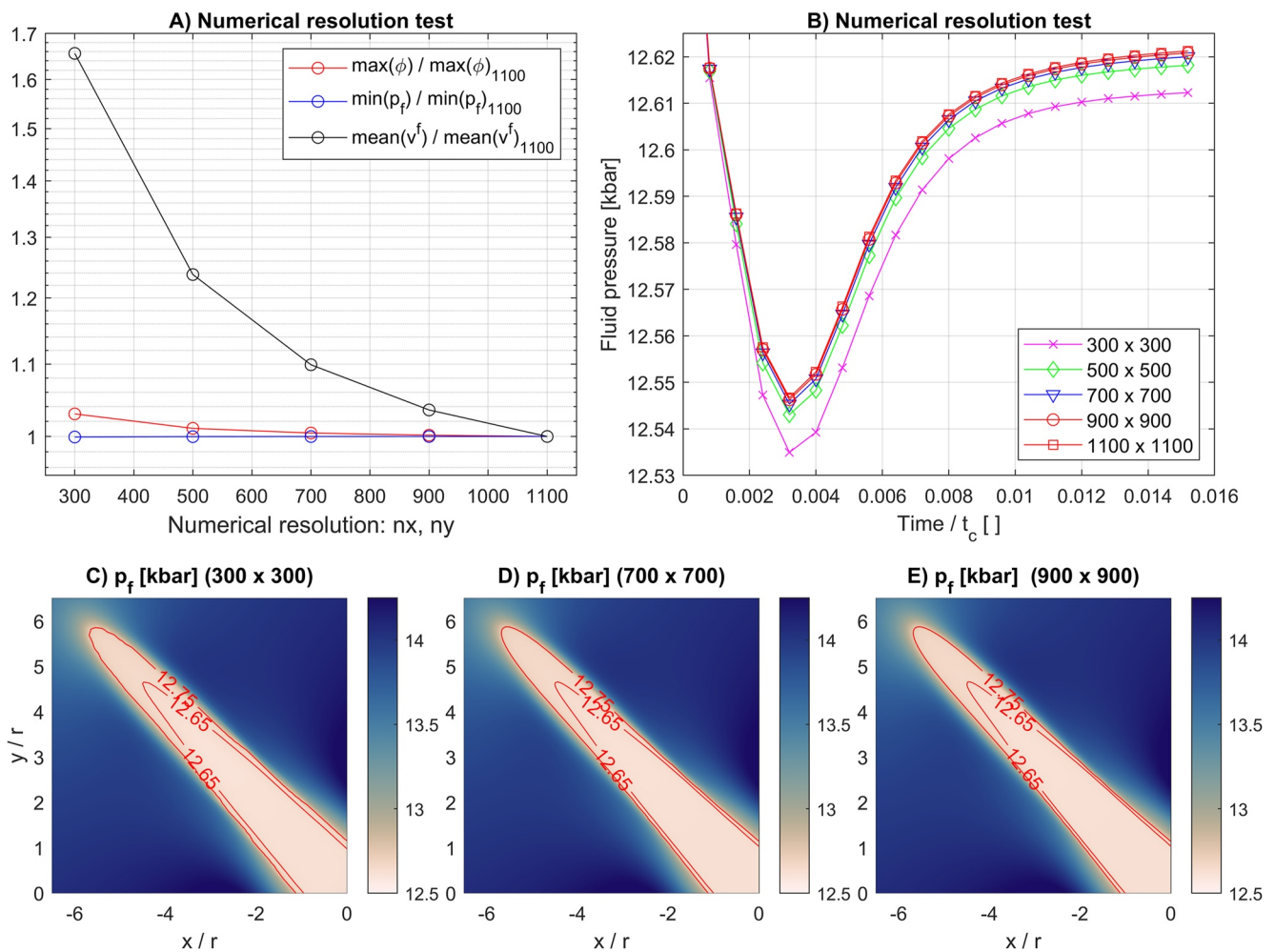


Figure A2. Numerical resolution test for the reference simulation S1. (a) For a dimensionless model time of 0.0152, the ratio of the maximum porosity in the model domain divided by the maximum porosity for a simulation with a resolution of $1,100 \times 1,100$ grid points is plotted vs. the corresponding resolution for simulations with different resolution. Similar ratios are plotted for the minimum fluid pressure in the model domain and the mean value of the fluid velocity. The larger the resolution, the less the three ratios vary. (b) Evolution of minimum fluid pressure in the model domain with time for different numerical resolutions (see legend). With larger resolution, the evolution of fluid pressure varies less. Panels (c–e): At a dimensionless model time of 0.0152, the colormap of the fluid pressure is displayed for three different resolutions (see numbers in panel titles). Two contour lines of fluid pressure are displayed for better comparability. A resolution of 900×900 was applied in the simulations presented in the main text.

(Figures A2c–A2e). For numerical resolutions of 300×300 , 700×700 , and 900×900 the contours of p_f are smooth and the colormaps of p_f are similar (Figures A2c–A2e). The numerical resolution test shows that the applied numerical model provides results which converge for increasing numerical resolution and are, hence, not dependent on the numerical resolution. For the presented numerical simulations, a numerical resolution of 900×900 was applied.

We also present a test for the numerical accuracy of the applied iterative PT solver. If the partial differential equations are solved correctly, then the left-hand sides of Equation A2 are zero. However, since these equations are solved with numerical approximations, the value of the left-hand side of the numerical form of Equation A2 is not exactly equal to zero. The deviation from zero is typically called a residual. During the iterative solution, iterations are performed until all residuals at all numerical grid points for all equations decrease below a certain tolerance value. We calculated the first time step for simulation S1 for different values of the tolerance (Figure A3). We choose three representative quantities to test their change with a change of the tolerance. These quantities are the minimum fluid pressure in the model domain, the maximal total pressure in the model domain and the maximal value of the second invariant of the deviatoric stress tensor (Figure A3). All three quantities stop changing once the tolerance decreases below a value of 10^{-6} . The results presented in Figure A3 show the convergence of the results with decreasing tolerance. A tolerance of 10^{-6} was applied in the presented simulations.

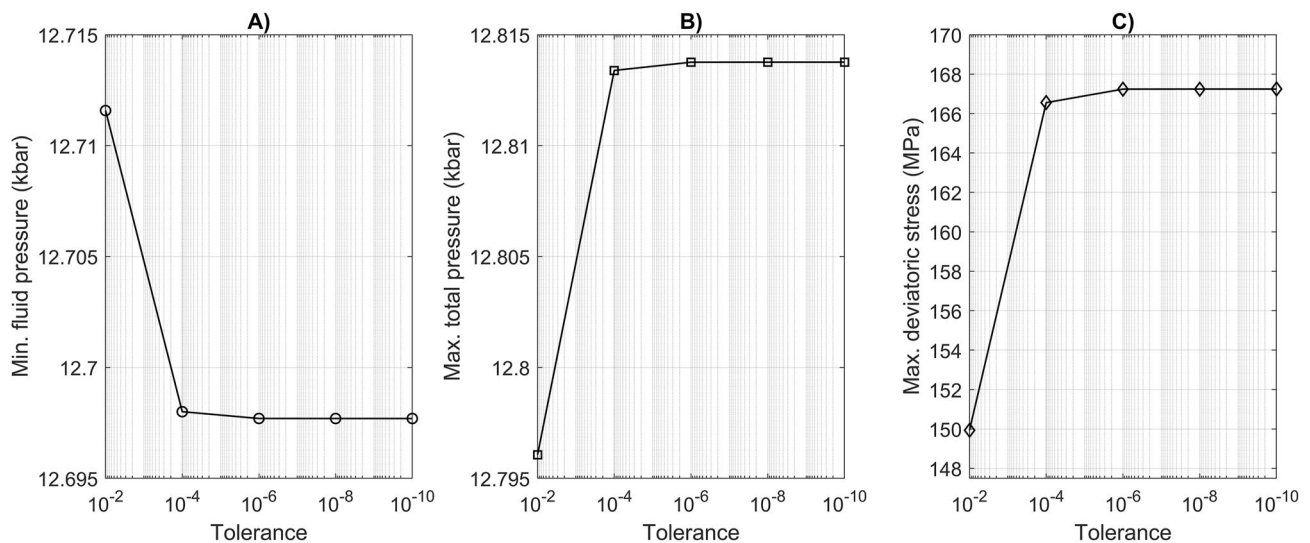


Figure A3. Numerical accuracy test for the reference simulation S1 after the first numerical time step. (a) The minimum value of the fluid pressure in the model domain vs. the applied tolerance of the iterative pseudo-transient solver. (b) Maximum value of total pressure vs. tolerance. (c) Maximum value of second invariant of deviatoric stress tensor versus tolerance. Once the tolerance is equal or smaller than 10^{-6} the three numerical values do not change anymore. A tolerance of 10^{-6} was used in the presented simulations.

Conflict of Interest

The authors declare no conflicts of interest relevant to this study.

Data Availability Statement

Software - The software developed and used in the scope of this study is licensed under MIT License. Repository name: The latest version of the numerical algorithm is available for download from GitHub at: <https://github.com/PTsolvers/PseudoTransientHMC.jl>. Past and future versions of the software are available from a permanent DOI repository (Zenodo) at: <https://zenodo.org/record/8367377> (Schmalholz & Räss, 2023). The codes are written using the Julia programming language and execute on graphical processing units. Refer to the repository's README for additional information.

Acknowledgments

We thank T. Keller, three anonymous reviewers and the Editors for their comments and suggestions. S.M.S. thanks Y. Podladchikov for theoretical advice, T. Duretz for programming advice, and M. Sirdey and F. Calvo for support in using the Curnagl cluster of the University of Lausanne. This work was supported by the University of Lausanne and the Swiss Geocomputing Centre. E.M. acknowledges the Johannes Gutenberg University of Mainz for financial support. L.R. acknowledges financial support from the Swiss University Conference and the Swiss Council of Federal Institutes of Technology through the Platform for Advanced Scientific Computing (PASC) program, obtained via the PASC project GPU4GEO. O.M. is grateful for scientific discussions with M. Scambelluri and J. Hermann in the field, where the idea of weak olivine veins was born 30 years ago.

References

- Aharonov, E., Spiegelman, M., & Kelemen, P. (1997). Three-dimensional flow and reaction in porous media: Implications for the Earth's mantle and sedimentary basins. *Journal of Geophysical Research*, *102*(B7), 14821–14833. <https://doi.org/10.1029/97jb00996>
- Aharonov, E., Whitehead, J., Kelemen, P., & Spiegelman, M. (1995). Channeling instability of upwelling melt in the mantle. *Journal of Geophysical Research*, *100*(B10), 20433–20450. <https://doi.org/10.1029/95jb01307>
- Audet, P., Bostock, M. G., Christensen, N. I., & Peacock, S. M. (2009). Seismic evidence for overpressured subducted oceanic crust and megathrust fault sealing. *Nature*, *457*(7225), 76–78. <https://doi.org/10.1038/nature07650>
- Baltzell, C., Parmentier, E. M., Liang, Y., & Tirupathi, S. (2015). A high-order numerical study of reactive dissolution in an upwelling heterogeneous mantle: 2. Effect of shear deformation. *Geochemistry, Geophysics, Geosystems*, *16*(11), 3855–3869. <https://doi.org/10.1002/2015gc006038>
- Bebout, G. E. (2014). Chemical and isotopic cycling in subduction zones. In H. D. Holland & K. K. Turekian (Eds.), *Treatise on Geochemistry* (pp. 703–747). Elsevier.
- Behr, W. M., & Bürgmann, R. (2021). Whats down there? The structures, materials and environment of deep-seated tremor and slip. *Philosophical Transactions of the Royal Society A*, *379*(2193), 20200218. <https://doi.org/10.1098/rsta.2020.0218>
- Beinlich, A., John, T., Vrijmoed, J., Tominaga, M., Magna, T., & Podladchikov, Y. (2020). Instantaneous rock transformations in the deep crust driven by reactive fluid flow. *Nature Geoscience*, *13*(4), 307–311. <https://doi.org/10.1038/s41561-020-0554-9>
- Bessat, A., Pilet, S., Podladchikov, Y. Y., & Schmalholz, S. M. (2022). Melt migration and chemical differentiation by reactive porosity waves. *Geochemistry, Geophysics, Geosystems*, *23*(2), e2021GC009963. <https://doi.org/10.1029/2021gc009963>
- Bloch, W., John, T., Kummerow, J., Salazar, P., Krüger, O. S., & Shapiro, S. A. (2018). Watching dehydration: Seismic indication for transient fluid pathways in the oceanic mantle of the subducting Nazca slab. *Geochemistry, Geophysics, Geosystems*, *19*(9), 3189–3207. <https://doi.org/10.1029/2018GC007703>
- Brantut, N., Sulem, J., & Schubnel, A. (2011). Effect of dehydration reactions on earthquake nucleation: Stable sliding, slow transients, and unstable slip. *Journal of Geophysical Research*, *116*(B5), B05304. <https://doi.org/10.1029/2010jb007876>
- Burlini, L., Di Toro, G., & Meredith, P. (2009). Seismic tremor in subduction zones: Rock physics evidence. *Geophysical Research Letters*, *36*(8), L08305. <https://doi.org/10.1029/2009gl037735>
- Chernak, L. J., & Hirth, G. (2010). Deformation of antigorite serpentinite at high temperature and pressure. *Earth and Planetary Science Letters*, *296*(1–2), 23–33. <https://doi.org/10.1016/j.epsl.2010.04.035>
- Chorin, A. J. (1997). A numerical method for solving incompressible viscous flow problems. *Journal of Computational Physics*, *135*(2), 118–125. <https://doi.org/10.1006/jcph.1997.5716>
- Connolly, J. (1990). Multivariable phase diagrams; an algorithm based on generalized thermodynamics. *American Journal of Science*, *290*(6), 666–718. <https://doi.org/10.2475/ajs.290.6.666>
- Connolly, J. (1997). Devolatilization-generated fluid pressure and deformation-propagated fluid flow during prograde regional metamorphism. *Journal of Geophysical Research*, *102*(B8), 18149–18173. <https://doi.org/10.1029/97jb00731>
- Connolly, J. (2005). Computation of phase equilibria by linear programming: A tool for geodynamic modeling and its application to subduction zone decarbonation. *Earth and Planetary Science Letters*, *236*(1–2), 524–541. <https://doi.org/10.1016/j.epsl.2005.04.033>
- Connolly, J. (2009). The geodynamic equation of state: What and how. *Geochemistry, Geophysics, Geosystems*, *10*(10), Q10014. <https://doi.org/10.1029/2009gc002540>
- Costa, A. (2006). Permeability-porosity relationship: A reexamination of the Kozeny-Carman equation based on a fractal pore-space geometry assumption. *Geophysical Research Letters*, *33*(2), L02318. <https://doi.org/10.1029/2005gl025134>
- Cruz-Atienza, V. M., Villafuerte, C., & Bhat, H. S. (2018). Rapid tremor migration and pore-pressure waves in subduction zones. *Nature Communications*, *9*(1), 2900. <https://doi.org/10.1038/s41467-018-05150-3>
- Dahlen, F. A. (1992). Metamorphism of nonhydrostatically stressed rocks. *American Journal of Science*, *292*(3), 184–198. <https://doi.org/10.2475/ajs.292.3.184>
- David, C., Wong, T.-F., Zhu, W., & Zhang, J. (1994). Laboratory measurement of compaction-induced permeability change in porous rocks: Implications for the generation and maintenance of pore pressure excess in the crust. *Pure and Applied Geophysics*, *143*(1–3), 425–456. <https://doi.org/10.1007/bf00874337>
- David, E. C., Brantut, N., Hansen, L. N., & Mitchell, T. M. (2018). Absence of stress-induced anisotropy during brittle deformation in antigorite serpentinite. *Journal of Geophysical Research: Solid Earth*, *123*(12), 10616–10644. <https://doi.org/10.1029/2018jb016255>
- Dohmen, J., & Schmeling, H. (2021). Magma ascent mechanisms in the transition regime from solitary porosity waves to diapirism. *Solid Earth*, *12*(7), 1549–1561. <https://doi.org/10.5194/se-12-1549-2021>
- England, P. (2018). On shear stresses, temperatures, and the maximum magnitudes of earthquakes at convergent plate boundaries. *Journal of Geophysical Research: Solid Earth*, *123*(8), 7165–7202. <https://doi.org/10.1029/2018jb015907>
- England, P. C., & Smye, A. J. (2023). Metamorphism and deformation on subduction interfaces: 1. *Physical Framework, Geochemistry, Geophysics, Geosystems*, *24*(1), e2022GC010644.

- Evans, B. W. (2004). The serpentinite multisystem revisited: Chrysotile is metastable. *International Geology Review*, 46(6), 479–506. <https://doi.org/10.2747/0020-6814.46.6.479>
- Evans, O., Spiegelman, M., & Kelemen, P. B. (2018). A poroelastic model of serpentinization: Exploring the interplay between rheology, surface energy, reaction, and fluid flow. *Journal of Geophysical Research: Solid Earth*, 123(10), 8653–8675. <https://doi.org/10.1029/2017jb015214>
- Evans, O., Spiegelman, M., & Kelemen, P. B. (2020). Phase-field modeling of reaction-driven cracking: Determining conditions for extensive olivine serpentinization. *Journal of Geophysical Research: Solid Earth*, 125(1), e2019JB018614. <https://doi.org/10.1029/2019jb018614>
- Fowler, A. C. (1985). A mathematical model of magma transport in the asthenosphere. *Geophysical & Astrophysical Fluid Dynamics*, 33(1–4), 63–96. <https://doi.org/10.1080/03091928508245423>
- Frank, W. B., Shapiro, N. M., Husker, A. L., Kostoglodov, V., Bhat, H. S., & Carnpillo, M. (2015). Along-fault pore-pressure evolution during a slow-slip event in Guerrero, Mexico. *Earth and Planetary Science Letters*, 413, 135–143. <https://doi.org/10.1016/j.epsl.2014.12.051>
- Gomberg, J., Cascadia, & Group, B. W. (2010). Slow-slip phenomena in Cascadia from 2007 and beyond: A review. *Bulletin*, 122(7–8), 963–978. <https://doi.org/10.1130/b30287.1>
- Hacker, B. R., Peacock, S. M., Abers, G. A., & Holloway, S. D. (2003). Subduction factory 2. Are intermediate-depth earthquakes in subducting slabs linked to metamorphic dehydration reactions? *Journal of Geophysical Research*, 108(B1), 2030. <https://doi.org/10.1029/2001jb001129>
- Halter, W. R., Macherel, E., & Schmalholz, S. M. (2022). A simple computer program for calculating stress and strain rate in 2D viscous inclusion-matrix systems. *Journal of Structural Geology*, 160, 104617. <https://doi.org/10.1016/j.jsg.2022.104617>
- Hatakeyama, K., Katayama, I., Hirauchi, K.-I., & Michibayashi, K. (2017). Mantle hydration along outer-rise faults inferred from serpentinite permeability. *Scientific Reports*, 7(1), 13870. <https://doi.org/10.1038/s41598-017-14309-9>
- Hebert, L. B., Antoshechkina, P., Asimow, P., & Gurnis, M. (2009). Emergence of a low-viscosity channel in subduction zones through the coupling of mantle flow and thermodynamics. *Earth and Planetary Science Letters*, 278(3–4), 243–256. <https://doi.org/10.1016/j.epsl.2008.12.013>
- Hermann, J., Müntener, O., & Scambelluri, M. (2000). The importance of serpentinite mylonites for subduction and exhumation of oceanic crust. *Tectonophysics*, 327(3–4), 225–238. [https://doi.org/10.1016/s0040-1951\(00\)00171-2](https://doi.org/10.1016/s0040-1951(00)00171-2)
- Hilaliet, N., Reynard, B., Wang, Y. B., Daniel, I., Merkel, S., Nishiyama, N., & Petigirard, S. (2007). High-pressure creep of serpentine, interseismic deformation, and initiation of subduction. *Science*, 318(5858), 1910–1913. <https://doi.org/10.1126/science.1148494>
- Hirauchi, K., Katayama, I., & Kouketsu, Y. (2020). Semi-brittle deformation of antigorite serpentinite under forearc mantle wedge conditions. *Journal of Structural Geology*, 140, 104151. <https://doi.org/10.1016/j.jsg.2020.104151>
- Hofmann, R., Xu, X., Batzle, M., Prasad, M., Furre, A.-K., & Pillitteri, A. (2005). Effective pressure or what is the effect of pressure? *The Leading Edge*, 24(12), 1256–1260. <https://doi.org/10.1190/l1.2149644>
- Holland, T., & Powell, R. (1998). An internally consistent thermodynamic data set for phases of petrological interest. *Journal of Metamorphic Geology*, 16(3), 309–343. <https://doi.org/10.1111/j.1525-1314.1998.00140.x>
- Holtzman, B., Groebner, N., Zimmerman, M., Ginsberg, S., & Kohlstedt, D. (2003). Stress-driven melt segregation in partially molten rocks. *Geochemistry, Geophysics, Geosystems*, 4(5). <https://doi.org/10.1029/2001gc000258>
- Hommel, J., Coltman, E., & Class, H. (2018). Porosity–permeability relations for evolving pore space: A review with a focus on (bio-) geochemically altered porous media. *Transport in Porous Media*, 124(2), 589–629. <https://doi.org/10.1007/s11242-018-1086-2>
- Huber, K., Vrijmoed, J. C., & John, T. (2022). Formation of olivine veins by reactive fluid flow in a dehydrating serpentinite. *Geochemistry, Geophysics, Geosystems*, 23(6), e2021GC010267. <https://doi.org/10.1029/2021GC010267>
- John, T., Gussone, N., Podladchikov, Y. Y., Bebout, G. E., Dohmen, R., Halama, R., et al. (2012). Volcanic arcs fed by rapid pulsed fluid flow through subducting slabs. *Nature Geoscience*, 5(7), 489–492. <https://doi.org/10.1038/ngeo1482>
- Jones, D. W. R., & Katz, R. F. (2018). Reaction-infiltration instability in a compacting porous medium. *Journal of Fluid Mechanics*, 852, 5–36. <https://doi.org/10.1017/jfm.2018.524>
- Karato, S. (2008). *Deformation of Earth materials*. Cambridge University Press.
- Kato, A., Iidaka, T., Ikuta, R., Yoshida, Y., Katsumata, K., Iwasaki, T., et al. (2010). Variations of fluid pressure within the subducting oceanic crust and slow earthquakes. *Geophysical Research Letters*, 37(14). <https://doi.org/10.1029/2010gl043723>
- Katz, R. F. (2008). Magma dynamics with the enthalpy method: Benchmark solutions and magmatic focusing at mid-ocean ridges. *Journal of Petrology*, 49(12), 2099–2121. <https://doi.org/10.1093/ptrology/egn058>
- Katz, R. F., Jones, D. W. R., Rudge, J. F., & Keller, T. (2022). Physics of melt extraction from the mantle: Speed and style. *Annual Review of Earth and Planetary Sciences*, 50(1), 507–540. <https://doi.org/10.1146/annurev-earth-032320-083704>
- Katz, R. F., Spiegelman, M., & Holtzman, B. (2006). The dynamics of melt and shear localization in partially molten aggregates. *Nature*, 442(7103), 676–679. <https://doi.org/10.1038/nature05039>
- Keller, T., & Katz, R. F. (2016). The role of volatiles in reactive melt transport in the asthenosphere. *Journal of Petrology*, 57(6), 1073–1108. <https://doi.org/10.1093/ptrology/egw030>
- Keller, T., May, D. A., & Kaus, B. J. (2013). Numerical modelling of magma dynamics coupled to tectonic deformation of lithosphere and crust. *Geophysical Journal International*, 195(3), 1406–1442. <https://doi.org/10.1093/gji/ggt306>
- Kempf, E. D., Hermann, J., Reusser, E., Baumgartner, L. P., & Lanari, P. (2020). The role of the antigorite + brucite to olivine reaction in subducted serpentinites (Zermatt, Switzerland). *Swiss Journal of Geosciences*, 113, 16. <https://doi.org/10.1186/s00015-020-00377-z>
- Kolditz, O., Shao, H., Wang, W., & Bauer, S. (2016). *Thermo-hydro-mechanical chemical processes in fractured porous media: Modelling and benchmarking* (p. 313). Springer. <https://doi.org/10.1007/978-3-319-11894-9>
- Labrousse, L., Hetenyi, G., Raimbourg, H., Jolivet, L., & Andersen, T. B. (2010). Initiation of crustal-scale thrusts triggered by metamorphic reactions at depth: Insights from a comparison between the Himalayas and Scandinavian Caledonides. *Tectonics*, 29(5), TC5002. <https://doi.org/10.1029/2009tc002602>
- Llana-Fúnez, S., Wheeler, J., & Faulkner, D. R. (2012). Metamorphic reaction rate controlled by fluid pressure not confining pressure: Implications of dehydration experiments with gypsum. *Contributions to Mineralogy and Petrology*, 164(1), 69–79. <https://doi.org/10.1007/s00410-012-0726-8>
- Malvoisin, B., Podladchikov, Y. Y., & Myasnikov, A. V. (2021). Achieving complete reaction while the solid volume increases: A numerical model applied to serpentinization. *Earth and Planetary Science Letters*, 563, 116859. <https://doi.org/10.1016/j.epsl.2021.116859>
- Malvoisin, B., Podladchikov, Y. Y., & Vrijmoed, J. C. (2015). Coupling changes in densities and porosity to fluid pressure variations in reactive porous fluid flow: Local thermodynamic equilibrium. *Geochemistry, Geophysics, Geosystems*, 16(12), 4362–4387. <https://doi.org/10.1002/2015gc006019>
- Matter, J. M., & Kelemen, P. B. (2009). Permanent storage of carbon dioxide in geological reservoirs by mineral carbonation. *Nature Geoscience*, 2(12), 837–841. <https://doi.org/10.1038/ngeo683>
- McKee, S., Tomé, M. F., Ferreira, V. G., Cuminato, J. A., Castelo, A., Sousa, F., & Mangiacavalli, N. (2008). The MAC method. *Computers & Fluids*, 37(8), 907–930. <https://doi.org/10.1016/j.compfluid.2007.10.006>

- McKenzie, D. (1984). The generation and compaction of partially molten rock. *Journal of Petrology*, 25(3), 713–765. <https://doi.org/10.1093/ptrology/25.3.713>
- Mei, S., Bai, W., Hiraga, T., & Kohlstedt, D. (2002). Influence of melt on the creep behavior of olivine–basalt aggregates under hydrous conditions. *Earth and Planetary Science Letters*, 201(3–4), 491–507. [https://doi.org/10.1016/s0012-821x\(02\)00745-8](https://doi.org/10.1016/s0012-821x(02)00745-8)
- Montesi, L. G. J., & Zuber, M. T. (2002). A unified description of localization for application to large-scale tectonics. *Journal of Geophysical Research*, 107(B3), ECV 1-1–ECV 1-21. <https://doi.org/10.1029/2001jb000465>
- Moulas, E., Burg, J.-P., & Podladchikov, Y. (2014). Stress field associated with elliptical inclusions in a deforming matrix: Mathematical model and implications for tectonic overpressure in the lithosphere. *Tectonophysics*, 631, 37–49. <https://doi.org/10.1016/j.tecto.2014.05.004>
- Moulas, E., & Schmalholz, S. M. (2020). The importance of interfacial instability for viscous folding in mechanically heterogeneous layers. *Geological Society, London, Special Publications*, 487(1), 45–58. <https://doi.org/10.1144/sp487.10>
- Omlin, S., Malvoisin, B., & Podladchikov, Y. Y. (2017). Pore fluid extraction by reactive solitary waves in 3-D. *Geophysical Research Letters*, 44(18), 9267–9275. <https://doi.org/10.1002/2017gl074293>
- Padrón-Navarta, J. A., Sánchez-Vizcaíno, V. L., Hermann, J., Connolly, J. A., Garrido, C. J., Gómez-Pugnaire, M. T., & Marchesi, C. (2013). Tschermak's substitution in antigorite and consequences for phase relations and water liberation in high-grade serpentinites. *Lithos*, 178, 186–196. <https://doi.org/10.1016/j.lithos.2013.02.001>
- Pandey, S. N., Vishal, V., & Chaudhuri, A. (2018). Geothermal reservoir modeling in a coupled thermo-hydro-mechanical-chemical approach: A review. *Earth-Science Reviews*, 185, 1157–1169. <https://doi.org/10.1016/j.earscirev.2018.09.004>
- Patankar, S. (2018). *Numerical heat transfer and fluid flow*. Taylor & Francis.
- Peacock, S. M. (1990). Fluid processes in subduction zones. *Science*, 248(4953), 329–337. <https://doi.org/10.1126/science.248.4953.329>
- Peng, Z. G., & Gombert, J. (2010). An integrated perspective of the continuum between earthquakes and slow-slip phenomena. *Nature Geoscience*, 3(9), 599–607. <https://doi.org/10.1038/ngeo940>
- Peters, D., Pettko, T., John, T., & Scambelluri, M. (2020). The role of brucite in water and element cycling during serpentinite subduction – Insights from Erro Tobbio (Liguria, Italy). *Lithos*, 360–361, 105431. <https://doi.org/10.1016/j.lithos.2020.105431>
- Pettko, T., & Bretscher, A. (2022). Fluid-mediated element cycling in subducted oceanic lithosphere: The orogenic serpentinite perspective. *Earth-Science Reviews*, 225, 103896. <https://doi.org/10.1016/j.earscirev.2021.103896>
- Plümpner, O., John, T., Podladchikov, Y. Y., Vrijmoed, J. C., & Scambelluri, M. (2017). Fluid escape from subduction zones controlled by channel-forming reactive porosity. *Nature Geoscience*, 10(2), 150–156. <https://doi.org/10.1038/ngeo2865>
- Poulet, T., Karrech, A., Regenauer-Lieb, K., Fisher, L., & Schaub, P. (2012). Thermal–hydraulic–mechanical coupling with damage mechanics using ESCRIPTRT and ABAQUS. *Tectonophysics*, 526, 124–132. <https://doi.org/10.1016/j.tecto.2011.12.005>
- Poulet, T., Veveakis, M., Herwegh, M., Buckingham, T., & Regenauer-Lieb, K. (2014). Modeling episodic fluid-release events in the ductile carbonates of the Glarus thrust. *Geophysical Research Letters*, 41(20), 7121–7128. <https://doi.org/10.1002/2014gl061715>
- Räss, L., Duret, T., & Podladchikov, Y. (2019). Resolving hydromechanical coupling in two and three dimensions: Spontaneous channelling of porous fluids owing to decompaction weakening. *Geophysical Journal International*, 218(3), 1591–1616. <https://doi.org/10.1093/gji/ggz239>
- Räss, L., Kolyukhin, D., & Minakov, A. (2019). Efficient parallel random field generator for large 3-D geophysical problems. *Computers & Geosciences*, 131, 158–169. <https://doi.org/10.1016/j.cageo.2019.06.007>
- Räss, L., Utkin, I., Duret, T., Omlin, S., & Podladchikov, Y. Y. (2022). Assessing the robustness and scalability of the accelerated pseudo-transient method. *Geoscientific Model Development*, 15(14), 5757–5786. <https://doi.org/10.5194/gmd-15-5757-2022>
- Rupke, L. H., Morgan, J. P., Hort, M., & Connolly, J. A. D. (2004). Serpentine and the subduction zone water cycle. *Earth and Planetary Science Letters*, 223(1–2), 17–34. <https://doi.org/10.1016/j.epsl.2004.04.018>
- Scambelluri, M., Fiebig, J., Malaspina, N., Muntener, O., & Pettko, T. (2004). Serpentine subduction: Implications for fluid processes and trace-element recycling. *International Geology Review*, 46(7), 595–613. <https://doi.org/10.2747/0020-6814.46.7.595>
- Scambelluri, M., Muntener, O., Hermann, J., Piccardo, G. B., & Trommsdorff, V. (1995). Subduction of water into the mantle: History of an Alpine peridotite. *Geology*, 23(5), 459–462. [https://doi.org/10.1130/0091-7613\(1995\)023<0459:Sowitm>2.3.Co;2](https://doi.org/10.1130/0091-7613(1995)023<0459:Sowitm>2.3.Co;2)
- Scambelluri, M., Strating, E. H. H., Piccardo, G. B., Vissers, R. L. M., & Rampone, E. (1991). Alpine olivine-bearing and titanium clinohumite-bearing assemblages in the Erro Tobbio peridotite (Voltri-Massif, NW Italy). *Journal of Metamorphic Geology*, 9(1), 79–91. <https://doi.org/10.1111/j.1525-1314.1991.tb00505.x>
- Schiemenz, A., Liang, Y., & Parmentier, E. M. (2011). A high-order numerical study of reactive dissolution in an upwelling heterogeneous mantle-I. Channelization, channel lithology and channel geometry. *Geophysical Journal International*, 186(2), 641–664. <https://doi.org/10.1111/j.1365-246X.2011.05065.x>
- Schmalholz, S. M., & Fletcher, R. C. (2011). The exponential flow law applied to necking and folding of a ductile layer. *Geophysical Journal International*, 184(1), 83–89. <https://doi.org/10.1111/j.1365-246X.2010.04846.x>
- Schmalholz, S. M., Moulas, E., Plümpner, O., Myasnikov, A. V., & Podladchikov, Y. Y. (2020). 2D hydro-mechanical-chemical modeling of (de)hydration reactions in deforming heterogeneous rock: The periclase-brucite model reaction. *Geochemistry, Geophysics, Geosystems*, 21(11), e2020GC009351. <https://doi.org/10.1029/2020gc009351>
- Schmalholz, S. M., & Räss, L. (2023). Ptsolvers/PseudoTransientHMC.jl: PseudoTransientHMC.jl 0.3.0 (v0.3.0) [Software]. Zenodo. <https://doi.org/10.5281/zenodo.8367377>
- Schmeling, H., Kruse, J. P., & Richard, G. (2012). Effective shear and bulk viscosity of partially molten rock based on elastic moduli theory of a fluid filled poroelastic medium. *Geophysical Journal International*, 190(3), 1571–1578. <https://doi.org/10.1111/j.1365-246X.2012.05596.x>
- Schmid, D. W., & Podladchikov, Y. Y. (2003). Analytical solutions for deformable elliptical inclusions in general shear. *Geophysical Journal International*, 155(1), 269–288. <https://doi.org/10.1046/j.1365-246x.2003.02042.x>
- Scott, T., & Kohlstedt, D. (2006). The effect of large melt fraction on the deformation behavior of peridotite. *Earth and Planetary Science Letters*, 246(3–4), 177–187. <https://doi.org/10.1016/j.epsl.2006.04.027>
- Shelly, D. R., Beroza, G. C., & Ide, S. (2007). Non-volcanic tremor and low-frequency earthquake swarms. *Nature*, 446(7133), 305–307. <https://doi.org/10.1038/nature05666>
- Simpson, G., & Spiegelman, M. (2011). Solitary wave benchmarks in magma dynamics. *Journal of Scientific Computing*, 49(3), 268–290. <https://doi.org/10.1007/s10915-011-9461-y>
- Spiegelman, M. (2003). Linear analysis of melt band formation by simple shear. *Geochemistry, Geophysics, Geosystems*, 4(9), 8615. <https://doi.org/10.1029/2002gc000499>
- Spiegelman, M., Kelemen, P. B., & Aharonov, E. (2001). Causes and consequences of flow organization during melt transport: The reaction infiltration instability in compactible media. *Journal of Geophysical Research*, 106(B2), 2061–2077. <https://doi.org/10.1029/2000jb900240>
- Steeb, H., & Renner, J. (2019). Mechanics of poro-elastic media: A review with emphasis on foundational state variables. *Transport in Porous Media*, 130(2), 437–461. <https://doi.org/10.1007/s11242-019-01319-6>

- Stevenson, D. J. (1989). Spontaneous small-scale melt segregation in partial melts undergoing deformation. *Geophysical Research Letters*, *16*(9), 1067–1070. <https://doi.org/10.1029/g1016i009p01067>
- Sulem, J., & Famin, V. (2009). Thermal decomposition of carbonates in fault zones: Slip-weakening and temperature-limiting effects. *Journal of Geophysical Research*, *114*(B3), B03309. <https://doi.org/10.1029/2008jb006004>
- Taetz, S., John, T., Brocker, M., Spandler, C., & Stracke, A. (2018). Fast intraslab fluid-flow events linked to pulses of high pore fluid pressure at the subducted plate interface. *Earth and Planetary Science Letters*, *482*, 33–43. <https://doi.org/10.1016/j.epsl.2017.10.044>
- Tarling, M. S., Smith, S. A. F., & Scott, J. M. (2019). Fluid overpressure from chemical reactions in serpentinite within the source region of deep episodic tremor. *Nature Geoscience*, *12*(12), 1034–1042. <https://doi.org/10.1038/s41561-019-0470-z>
- Tsenn, M. C., & Carter, N. L. (1987). Upper limits of power law creep of rocks. *Tectonophysics*, *136*(1–2), 1–26. [https://doi.org/10.1016/0040-1951\(87\)90332-5](https://doi.org/10.1016/0040-1951(87)90332-5)
- Ulmer, P., & Trommsdorff, V. (1995). Serpentine stability to mantle depths and subduction-related magmatism. *Science*, *268*(5212), 858–861. <https://doi.org/10.1126/science.268.5212.858>
- Van Avendonk, H. J. A., Holbrook, W. S., Lizarralde, D., Mora, M. M., Harder, S., Bullock, A. D., et al. (2010). Seismic evidence for fluids in fault zones on top of the subducting Cocos Plate beneath Costa Rica. *Geophysical Journal International*, *181*(2), 997–1016. <https://doi.org/10.1111/j.1365-246X.2010.04552.x>
- Virieux, J. (1986). P-SV wave propagation in heterogeneous media: Velocity-stress finite-difference method. *Geophysics*, *51*(4), 889–901. <https://doi.org/10.1190/1.1442147>
- Wang, L. H., Yarushina, V. M., Alkhimenkov, Y., & Podladchikov, Y. (2022). Physics-inspired pseudo-transient method and its application in modelling focused fluid flow with geological complexity. *Geophysical Journal International*, *229*(1), 1–20. <https://doi.org/10.1093/gji/ggab426>
- Yarushina, V. M., & Podladchikov, Y. Y. (2015). (De)compaction of porous viscoelastoplastic media: Model formulation. *Journal of Geophysical Research: Solid Earth*, *120*(6), 4146–4170. <https://doi.org/10.1002/2014jb011258>